https://ntrs.nasa.gov/search.jsp?R=19660027737 2018-07-21T15:34:15+00:00Z

TECH LIBRARY KAFB, NM
0099441

NASA CONTRACTOR REPORT

NASA CR-584

LOAN COPY: RETURN TO
AFWL (WLIL-2)
KIRTLAND AFB, N MEX

CONVECTIVE AND RADIATIVE HEAT TRANSFER DURING SUPERORBITAL ENTRY

by H. Hoshizaki and K. H. Wilson

Prepared by
LOCKHEED AIRCRAFT CORPORATION
Palo Alto, Calif.
for Western Operations Office

NATIONAL AERONAUTICS AND SPACE ADMINISTRATION • WASHINGTON, D. C. • SEPTEMBER 1966

TECH LIBRARY KAFB, NM

0099441

NASA CR-584

CONVECTIVE AND RADIATIVE HEAT TRANSFER DURING SUPERORBITAL ENTRY

By H. Hoshizaki and K. H. Wilson

Distribution of this report is provided in the interest of information exchange. Responsibility for the contents resides in the author or organization that prepared it.

Prepared under Contract No. NAS 7-295 by
LOCKHEED AIRCRAFT CORPORATION
Palo Alto, Calif.

for Western Operations Office

NATIONAL AERONAUTICS AND SPACE ADMINISTRATION

For sale by the Clearinghouse for Federal Scientific and Technical Information
Springfield, Virginia 22151 – Price $2.50

FOREWORD

The work described in this report was completed for the National Aeronautics and Space Administration Headquarters, under the terms and specifications of their Contract NAS 7-295, issued through their Western Operations Office, 150 Pico Boulevard, Santa Monica, California – 90406.

The work was performed in the Aerospace Sciences Laboratory, R. D. Moffat, Manager, of the Lockheed Palo Alto Research Laboratory.

ABSTRACT

The convective and radiative heat transfer to vehicles entering planetary atmospheres at superorbital velocities is investigated. An integral method is employed to determine the radiative and convective heating around a blunt body. The effect of mass injection, radiative emission and absorption, radiation cooling, and coupling between convection and radiation are included in the analysis. The absorption coefficients of the shock-layer gas, as well as the injected ablation products are determined as a function of particle-number density, temperature, and radiation frequency. The results obtained show that self-absorption can reduce the radiative heating by an order of magnitude but has little effect on the convective heating. It was also found that the nose radius which results in the minimum total heat-transfer rate at the stagnation point is much larger (6 ft to 10 ft diam. at U_∞ = 50,000 fps) than the values indicated by an optically thin analysis. Furthermore, it is shown that the total stagnation-point heat-transfer rate is a very weak function of the nose radius, contrary to the results obtained from an optically thin analysis.

ACKNOWLEDGMENTS

The writers would like to express their sincere appreciation to W. E. Nicolet and L. E. Lasher of the laboratory for their helpful discussions and suggestions during the course of the work described in this report. Particular thanks are extended to H. R. Kirch for her many contributions in IBM code revisions, programming, and suggestions on the numerical analysis.

CONTENTS

Section		Page
	FOREWORD	iii
	ABSTRACT	v
	ACKNOWLEDGMENTS	vii
	ILLUSTRATIONS	x
	NOMENCLATURE	xi
1	INTRODUCTION	1
2	ANALYSIS	2
	2.1 General Method of Solution	2
	2.2 Governing Equations	3
	2.3 Velocity and Species Concentration Profiles and Boundary Conditions	9
3	GAS PROPERTIES	11
	3.1 Thermodynamic and Transport Properties	11
	3.2 Number Densities	11
	3.3 Absorption Coefficients	16
4	NUMERICAL METHOD	27
5	DISCUSSION OF RESULTS	28
	5.1 Comparison of Present Results to Previous Solutions	28
	5.2 Effect of Self-Absorption on Total Heating	28
	5.3 Effect of Self-Absorption on Nose Radius for Minimum Total Heating	36
	5.4 Heat Transfer Distribution	43
6	CONCLUSIONS	47
7	REFERENCES	48

ILLUSTRATIONS

Figure		Page
1	Body-Oriented Coordinate System	5
2	Equilibrium Composition of the Pyrolysis Products of Nylon-Phenolic (1.0-atm pressure)	12
3	Summary of Absorption Coefficients	17
4	Quantum Mechanical Correction Factor $\xi(h\nu)$	20
5	Comparison of Biberman and Armstrong Continuum Absorption Coefficients for Air	22
6	Effective Cross Section of Molecules	24
7	Comparison of Stagnation-Point Heat-Transfer Results	29
8	Stagnation Point Velocity, Enthalpy, and Concentration Profiles, $\bar{U} = 4.1$, $P_\delta = 1$ atm, $R = 1$ ft, $(\rho\nu)/\rho U)_\infty = 0.053$	30
9	Reduction of Convective Heating Due to Mass Injection	31
10	Summary of Stagnation Point Convective and Radiative Heat Transfer	33
11	Monochromatic Heat Flux, $\bar{U} = 3.45$, $\bar{h} = 20$, $R = 4$ ft, With Mass Injection, $(\rho v)_w/(\rho U)_\infty = 0.05$	36
12	Monochromatic Heat Flux, $\bar{U} = 5.0$, $\bar{h} = 2.0$, $R = 2$ ft	37
13	Heat Flux as a Function of Nose Radius, $\bar{U} = 3.45$, $\bar{h} = 2.0$, With Mass Injection, $(\rho v)_w/(\rho U)_\infty = 0.05$	39
14	Heat Flux as a Function of Nose Radius, $\bar{U} = 3.7$, $\bar{h} = 2.3$, No Mass Injection	40
15	Heat Flux as a Function of Nose Radius, $\bar{U} = 5.0$, $\bar{h} = 2.0$, No Mass Injection	41
16	Heat Flux as a Function of Nose Radius, $\bar{U} = 5.0$, $\bar{h} = 2.0$, With Mass Injection, $(\rho v)_w/(\rho U)_\infty = 0.05$	42
17	Convective and Radiative Heat-Transfer Distribution on a Hemisphere, $\bar{U} = 4.1$, $\bar{h} = 1.8$, $R = 1$ ft, 1st Iteration	44
18	Effect of Iteration on Heat-Transfer Distribution	45

NOMENCLATURE

A	Avogadro's number
a_i	velocity profile coefficients
C	mass fraction of injected species
C_p	total specific heat at constant pressure
$\bar{C}_p$	frozen specific heat at constant pressure
c	light velocity
D_{ij}	diffusion coefficient for a multicomponent system
E'	radiant emission per unit time per unit volume
$E_{B\nu}$	blackbody emissive power
$\mathcal{E}_n$	exponential function
f	velocity function, u/u_δ
H	total enthalpy
h	static enthalpy, also Planck constant
h_i	static enthalpy of ith species, including enthalpy of formation
$\bar{h}$	altitude in 10^5 ft
I_o	mass conservation integral
I_1	momentum-integral
k	quasi-total thermal conductivity, also Boltzmann constant
$\bar{k}$	frozen thermal conductivity
M_i	molecular weight of species i

M_o	molecular weight of undissociated gas
N	number density
n_i	moles of species i per unit volume
n_t	total number of moles per unit volume
P	static pressure
Pr	total Prandtl number, $Pr = C_p\mu/k$
$\dot{q}_c$	convective energy flux
$\dot{q}_r$	radiative energy flux
R	body radius
$\tilde{Re}$	Reynolds number, $\rho_{\delta,o}U_\infty R/\mu_\delta$
Re	Reynolds number, $\rho_{\delta,o}U_\infty R/\mu_{\delta,o}$
r	body radius measured from body centerline
S	distance along shock wave
Sc	Schmidt number
T	temperature
U_∞	free-stream velocity
$\bar{U}$	velocity in 10^4 fps
u	velocity component parallel to body
v	velocity component normal to surface
x, y	body-oriented coordinate system
α_{CO}	carbon monoxide mass fraction of ablation products
β	velocity gradient
γ	isentropic index
δ	shock detachment distance

$\tilde{\delta}$	transformed shock detachment distance
ϵ	difference between body and shock angle
η	Dorodnitzyn variable
θ	body angle, also kT
κ	body curvature
$\tilde{\kappa}$	$1 + \kappa y$
κ_ν	absorption coefficient, cm^{-1}
μ	dynamic viscosity
ν	kinematic viscosity, also frequency
ξ	nondimensional surface distance, x/R
ρ	density
$\bar{\rho}$	density ratio across shock, ρ_∞/ρ_δ
σ	Stefan-Boltzmann constant
σ^*	effective cross-section, $\sigma^* = \kappa_\nu/N$
τ_v	monochromatic optical thickness
ϕ	shock angle
χ	$h\nu/kT$
ω	vorticity

Subscripts

a	atom
ad	adiabatic (no radiation loss)
CO	carbon monoxide molecule
C—O	carbon and oxygen atoms from dissociation of CO
e	electron

i	i^{th} chemical species, also ion
m	molecule
N_2	nitrogen molecule
N	nitrogen atom
O_2	oxygen molecule
O	oxygen atom
t	total
w	wall quantities
δ	quantities immediately behind shock
∞	free-stream condition
1	injected gas
2	air
0	stagnation point

Section 1
INTRODUCTION

The analysis presented in this report is an extension of a previous investigation carried out by the authors on convective and radiative heat transfer during superorbital entry (Ref. 1). In Ref. 1, the effect of radiation cooling on the convective and radiative heat flux and the coupling between these two modes of energy transfer were investigated for an optically thin shock layer. In the present report, the previous analysis (Ref. 1) has been extended to include mass injection of ablation products into the shock layer and self-absorption of radiant energy by molecules, atoms, and ions of both air and the products of ablation. The frequency dependence of the absorption coefficients is fully taken into account. The coupling between the convective and radiative heat transfer caused by radiation cooling and the transfer of energy by emission and absorption are accounted for by considering the entire shock layer, including the viscous region near the wall.

In the present analysis, shock-layer gas is assumed to be an inert binary mixture, in that chemical reactions between the products of ablation and air are not taken into account. The radiation from atomic lines has also been omitted in the calculation of the radiant energy transfer.

In the analysis to follow, some of the analytical details have been omitted since these details have been presented in the previous work (Ref. 1).

Section 2
ANALYSIS

2.1 GENERAL METHOD OF SOLUTION

The objective of this analysis is to determine the flow field and the convective and radiative heat transfer to an ablating body. The governing equations are first simplified by assuming the shock layer to be thin; i.e., $\delta << 1$. In addition, the viscous region is allowed to extend out to the shock wave which defines the lower limit in Reynolds number. The shock wave itself is assumed to be a discontinuity. The simplified equations are solved by means of a combined integral-finite difference method. The momentum and species continuity equations are integrated across the shock layer to obtain integro-differential equations in one independent variable. The integrals are evaluated by assuming that the velocity and concentration profiles in the shock layer can be represented by suitable polynomials. The energy equation is solved by means of a finite difference method (Ref. 2) using the velocity and concentration profiles from the integral solution of the momentum and species continuity equations.

The solution at points other than the stagnation point presents some difficulties since the symmetry conditions at the stagnation point yield all but one necessary boundary condition to treat the problem as an initial value problem. The unknown boundary condition is either the stagnation-point shock detachment distance or the shock curvature. In the present analysis, solutions are obtained by an iteration procedure. An initial guess is made for the shock angle as a function of body position. The equations are then solved to obtain a complete description of the shock-layer flow field. A new shock shape is computed which forms the basis of the second iteration. The procedure is repeated until satisfactory convergence is obtained.

2.2 GOVERNING EQUATIONS

The governing equations are obtained by simplifying the complete conservation equations (Ref. 3) for a multicomponent, continuum gas in thermodynamic equilibrium. Both the thin-shock approximations and boundary-layer-type approximations are used in an order-of-magnitude analysis to reduce the complete equations to a set of equations which are corret to $O(\bar{\rho})$.

The governing equations valid to $O(\bar{\rho})$ are

x-momentum

$$\left(\frac{r'}{r'_w}\right)^n \rho'\tilde{\kappa}'\left[u'\frac{\partial u'}{\partial x'} + \tilde{\kappa}'v'\frac{\partial u'}{\partial y'} + \kappa'u'v'\right] = -\frac{\partial P'}{\partial x'} + \frac{\partial}{\partial y'}\left[\left\{\left(\frac{r'}{r'_w}\right)^n + 2\kappa'y'\right\}\mu'\frac{\partial u'}{\partial y'} - \kappa'\mu'u'\right] \tag{1}$$

y-momentum

$$\rho'\kappa'u'^2 = \frac{\partial P'}{\partial y'} \tag{2}$$

energy

$$\rho'\left(\frac{r'}{r'_w}\right)^n\left[u'\frac{\partial H'}{\partial x'} + \tilde{\kappa}'v'\frac{\partial H'}{\partial y'}\right] = \frac{\partial}{\partial y'}\left[\frac{\mu'}{\tilde{\kappa}'}\left\{\left(\frac{r'}{r'_w}\right)^n + 2\kappa'y'\right\}\left\{\frac{\partial H'}{\partial y'} + \left(\frac{1}{Pr} - 1\right)\frac{\partial h'}{\partial y'}\right\}\right.$$

$$\left. + \frac{\partial}{\partial y'}\left[\left(\frac{r'}{r'_w}\right)^n \tilde{\kappa}'\rho'\sum_i D_{ij}h'_i\frac{\partial C_i}{\partial y'}\right] - \kappa'\frac{\partial}{\partial y'}(\mu'u'^2) - \tilde{\kappa}'\left(\frac{r'}{r'_w}\right)^n E' \right. \tag{3}$$

$$E' = -\int_0^\infty \kappa'_\nu(\tau_\nu)\left\{\int_0^{\tau_{\nu s}} 2E'_{B\nu}(t)\mathcal{E}_1(|t - \tau_\nu|)\,dt - 4E'_{B\nu}(\tau_\nu)\right\}d\nu$$

$$E'_{B\nu} = \pi\frac{2h\nu^3}{c^2}\frac{1}{[e^{h\nu/kT} - 1]} \quad , \quad \mathcal{E}_n(f) = \int_0^\infty \frac{e^{-f\omega}}{\omega^n}\,d\omega$$

global continuity

$$\frac{\partial}{\partial x'}\left(r'^{n}\rho' u'\right) + \frac{\partial}{\partial y'}\left(r'^{n}\tilde{\kappa}'\,\rho' v'\right) = 0 \tag{4}$$

species continuity

$$\left(\frac{r'}{r'_w}\right)^{n}\rho' u'\,\frac{\partial C}{\partial x'} + \left(\frac{r'}{r'_w}\right)^{n}\rho' v'\tilde{\kappa}'\,\frac{\partial C}{\partial y} = \frac{\partial}{\partial y'}\left[\left(\frac{r'}{r'_w}\right)^{n}\frac{\tilde{\kappa}'\mu'}{S_c}\,\frac{\partial C}{\partial y'}\right] \tag{5}$$

where $n = 0$ for planar bodies and $n = 1$ for axisymmetric bodies and primes indicate dimensional quantities.

The body-oriented coordinate system used is shown in Fig. 1. An important assumption made in the present analysis is that the injected gas does not react chemically with air. The gas in the shock layer is assumed to be an inert binary mixture of air and injected gas. Dissociation and ionization effects on the thermodynamic and transport properties of the mixture are accounted for by use of a quasi-total property concept. The properties which appear in the governing equations are for the mixture (dissociated and/or ionized air plus injected species). The reaction thermal conductivity, which represents transport of energy by diffusion of species, is assumed to be separable into diffusion among all species of air and the diffusion between the injected gas and air. That part of the reaction thermal conductivity which represents diffusion among the air species is added to the mixture frozen thermal conductivity to obtain a quasi-total thermal conductivity. In the energy equation, the diffusion between the injected gas and air is taken into account by the diffusion term. The advantage of this approach, in contrast to the use of a true total thermal conductivity, is that the total mixture conductivity need not be calculated in advance for arbitrary pressures, temperatures, and composition.

The Prandtl number which appears in the energy equation is composed of the total specific heat and viscosity of the mixture and the quasi-total thermal conductivity.

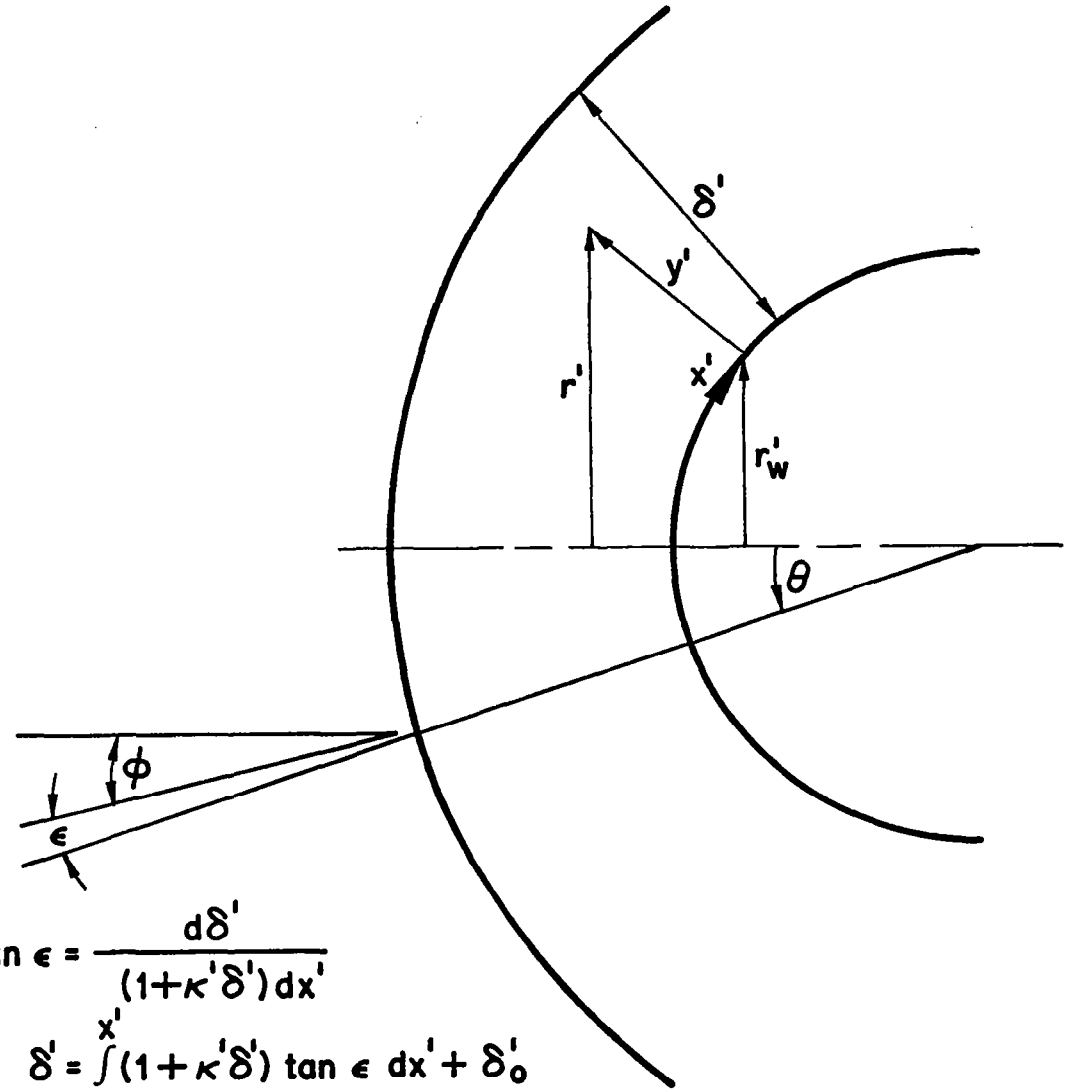

$$\tan \epsilon = \frac{d\delta'}{(1+\kappa'\delta')\,dx'}$$

$$\delta' = \int_0^{x'} (1+\kappa'\delta') \tan \epsilon \; dx' + \delta'_0$$

$$r' = r'_w + y' \sin \theta$$

Fig. 1 Body-Oriented Coordinate System

The radiation term, E', is the net emission or absorption of radiant energy per unit volume per unit time. It is a function of the absorption coefficient which, in turn, is dependent on the species number density, the radiation wavelength, temperature, and geometry. In this analysis, the tangent slab approximation has been made so that the radiation term is only a function of one spatial coordinate (y). The gray-gas approximation is not made in this analysis since it has been amply demonstrated in Ref. 4 that such an approximation can yield quantitative results which are in error by as much as an order of magnitude.

In the analysis to follow, the variables are nondimensionalized in the following manner:

$$u = \frac{u'}{U'_\infty} \qquad \xi = \frac{x'}{R'} \qquad \delta = \frac{\delta'}{R'} \qquad (\rho\, v)_w = \frac{(\rho' v')_w}{\rho_\infty U_\infty}$$

$$v = \frac{v'}{U'_\infty} \qquad y = \frac{y'}{R'} \qquad \tilde{\delta} = \frac{\tilde{\delta}'}{R'} \qquad h_\delta = \frac{h'_\delta}{U_\infty^2/2}$$

$$E = \frac{E'R'}{\rho'(U'_\infty)^3} \qquad \rho = \frac{\rho'}{\rho'_{\delta,o}} \qquad \mu = \frac{\mu'}{\mu'_{\delta,o}}$$

$$\kappa = \kappa' R' \qquad H = \frac{H'}{H'_\delta} \qquad P = \frac{P'}{\rho'_\infty U'^2_\infty}$$

$$\tilde{\kappa} = 1 + \kappa y \qquad h = \frac{h'}{h_\delta} \qquad r = \frac{r'}{R'}$$

The compressibility effects can be reduced significantly by introducing the Dorodnitzyn variable defined by

$$\eta = \frac{\int_o^{y'} (r'/r'_w)^n \rho' \, dy'}{\int_o^{\delta} (r'/r'_w)^n \rho' \, dy} \tag{6}$$

Integration across the shock layer of the momentum and species continuity equations and transformation into the η, ξ variables results in the following integro-differential equations. The momentum equation is integrated from the wall to the shock while the species continuity equation is integrated from the wall to the edge of the injected gas layer, δ_c.

momentum

$$\frac{dI_1}{d\xi} + \left[\frac{2}{u_\delta}\frac{du_\delta}{d\xi} + \frac{n}{r_w}\frac{dr_w}{d\xi}(1 + \delta\kappa)\right]I_1 - \left(1 + \frac{n\delta \sin\theta}{r_w}\right)\rho_\delta \frac{d\delta}{d\xi}$$

$$- \frac{d\kappa}{d\xi}\tilde{\delta}^2 \int_0^1 \left(f^2 \int_0^\eta \frac{d\bar{\eta}}{\rho}\right) d\eta + \left[1 + \delta\left(\frac{n \sin\theta}{r_w} + 2\kappa\right)\right]\frac{v_\delta}{u_\delta}$$

$$= -\frac{\delta\bar{\rho}_o}{u_\delta^2}\left(\frac{\partial P}{\partial \xi}\right)_\delta + \frac{1}{\tilde{\delta} u_\delta \mathrm{Re}}\left[\left\{1 + 2\delta\left(\frac{n \sin\theta}{r_w} + \kappa\right)\right\}(\rho\mu)_\delta f'(1) - \mu_\delta \tilde{\delta}\kappa - (\rho\mu)_w f'(0)\right] \quad (7)$$

species continuity

$$\frac{dI_2}{d\xi} + \left(\frac{1}{u_\delta}\frac{du_\delta}{d\xi} + \frac{n}{r_w}\frac{dr_w}{d\xi}\right)I_2 + C(1)\left(\frac{r_\delta}{r_w}\right)^n\left(\tilde{\kappa}_\delta \frac{v_\delta}{u_\delta} - \frac{d\delta}{d\xi}\right)$$

$$= \frac{1}{\tilde{\delta}\mathrm{Re}}\left[\left(\frac{r_\delta}{r_w}\right)^{2n}\frac{\tilde{\kappa}_\delta}{Sc_\delta}\frac{(\rho\mu)_{\delta_c}}{(\rho\mu)_{\delta,o}}C'(\eta_c) - \frac{1}{Sc_w}\frac{(\rho\mu)_w}{(\rho\mu)_{\delta,o}}C'(0)\right] \quad (8)$$

where

$$I_1 = \tilde{\delta}\int_0^1 f^2\, d\eta \quad , \quad I_2 = \tilde{\delta}\int_0^{\eta_c} fC\, d\eta$$

$$f = u/u_\delta \qquad C = \rho_1/\rho_t \qquad (9a-9d)$$

η_c is the transformed injected gas layer thickness, and primes on f and C denote differentiation. In addition, the following approximation was used to obtain the second term in the momentum equation:

$$\tilde{\kappa}_\delta I_1 \approx \tilde{\delta} \int_o^1 \tilde{\kappa} f^2 \, dy'$$

In the transformed variables, the energy equation becomes

$$\left[\frac{\rho\mu}{Pr} \frac{1}{\tilde{\kappa}} \left(\frac{r}{r_w}\right)^n \left\{\left(\frac{r}{r_w}\right)^n + 2\kappa y\right\} g'\right]' + g' \tilde{\delta} \, Re \, u_\delta \left[\frac{\partial I_o}{\partial \xi} + I_o \frac{\partial/\partial\xi\left(u_\delta r_w^n\right)}{u_\delta r_w^n} - \rho v \frac{\bar{\rho}}{u_\delta}\right]$$

$$= Re \, \tilde{\delta} \, u_\delta f \frac{\partial g}{\partial \xi} + \left[2\rho\mu \frac{1}{\tilde{\kappa}} \left(\frac{r}{r_w}\right)^n \left\{\left(\frac{r}{r_w}\right)^n + 2\kappa y\right\} \left(\frac{1}{Pr} - 1\right) u_\delta^2 ff' - \left(\frac{r}{r_w}\right)^{2n} \tilde{\kappa}\rho\mu \frac{h_\delta}{H_\delta} \frac{1}{Sc} C' \left(\frac{h_1}{h_\delta} - \frac{h_2}{h_\delta}\right)\right]'$$

$$+ 2u_\delta \tilde{\delta}\kappa(\mu f^2)' + 2Re \, \tilde{\delta}^2 \tilde{\kappa} E \tag{10}$$

where the mass flux, normal to the surface, was replaced by the following expression obtained by integrating the global continuity equation.

$$\tilde{\delta} f \frac{\partial \eta}{\partial \xi} + \left(\frac{r}{r_w}\right)^n \tilde{\kappa} \frac{\rho v}{u_\delta} = - \frac{\partial I_o}{\partial \xi} - I_o \frac{\partial/\partial\xi\left(u_\delta r_w^n\right)}{u_\delta r_w^n} + \frac{\rho v}{u_\delta} \tag{11}$$

The quantity $I_o(\eta)$ is defined by

$$I_1 = \tilde{\delta} \int_o^\eta f \, d\eta \tag{12}$$

The $I_o(\eta)$ gradient in the streamwise direction is replaced by (Ref. 2)

$$\left(\frac{\partial I_o}{\partial \xi}\right)_i = (I_o)_i \left(\frac{1}{\xi_i - \xi_{i-1}} + \frac{1}{\xi_i - \xi_{i-2}}\right) + (I_o)_{i-1} \left[\frac{\xi_i - \xi_{i-2}}{(\xi_i - \xi_{i-1})(\xi_{i-1} - \xi_{i-2})}\right]$$

$$+ (I_o)_{i-2} \left[\frac{\xi_i - \xi_{i-1}}{(\xi_i - \xi_{i-2})(\xi_{i-1} - \xi_{i-2})}\right] \tag{13}$$

with a similar expression for $\partial I_1/\partial \xi$ and $\partial I_2/\partial \xi$. These gradients can now be evaluated at any point in the flow field in terms of the known solution at two previous upstream integration points. The enthalpy gradient in the streamwise direction is approximated by

$$\left(\frac{\partial g}{\partial \xi}\right)_i = \frac{g_i - g_{i-1}}{\Delta \xi}$$

2.3 VELOCITY AND SPECIES CONCENTRATION PROFILES AND BOUNDARY CONDITIONS

The velocity and species concentration profiles are assumed to be representable by polynomials in η where the coefficients are functions of the streamwise variable ξ. The coefficients are determined from boundary conditions applied at the wall and immediately behind the shock. The shock-boundary conditions are the usual Rankine-Hugoniot relations which can be expressed as follows:

$$u_\delta = \sin \phi \sin \epsilon + \bar{\rho} \cos \phi \sin \epsilon \tag{14a}$$

$$v_\delta = \sin \phi \sin \epsilon - \bar{\rho} \cos \phi \cos \epsilon \tag{14b}$$

$$P_\delta = (1 - \bar{\rho}) \cos^2 \phi \tag{14c}$$

Fifth- and second-order polynomials are used to represent the velocity and species concentration profiles, respectively.

$$\frac{u}{u_\delta} = f = \sum_{i=o}^{5} a_i \eta^i \tag{15}$$

$$\frac{\rho_1}{\rho_\delta} = C = \sum_{i=o}^{2} c_i \eta^i \tag{16}$$

Sufficient boundary conditions are specified so that the coefficients a_i and c_i can be expressed in terms of known quantities evaluated at the wall and behind the shock wave, and the shock detachment distance. The integrated momentum and species continuity equations are used to determine the shock detachment distance and the thickness of the injected gas layer within the shock layer, respectively. The six boundary conditions used to determine the velocity profile coefficients are as follows:

(1) $u = 0$, $\eta = 0$
(2) $u = 1$, $\eta = 1$
(3) $v = v_\delta$, $\eta = 1$
(4) Momentum equation evaluated at the wall
(5) $\omega = \omega_\delta$, $\eta = 1$
(6) $f'' = 0$, $\eta = 1$

The concentration profile coefficients are evaluated using the following three boundary conditions:

(1) Mass flux of air at the wall is zero $\rho_2' v' - \rho' D_{12} \, \partial C/\partial y' = 0$
(2) Species concentration equation evaluated at the wall
(3) $C = 0$ at $\eta = \eta_c$ where η_c is the transformed injected gas layer thickness

Section 3
GAS PROPERTIES

3.1 THERMODYNAMIC AND TRANSPORT PROPERTIES

The analysis up to this point is valid for any multicomponent gas in thermodynamic equilibrium. Numerical solutions can be obtained if the thermodynamic, transport, and radiative properties are known. In the present report, numerical results are obtained under the assumption that the thermodynamic and transport properties of the injected gas are identical to that of air. The thermodynamic and transport properties, as computed by Hansen (Ref. 5) and correlated by Viegas and Howe (Ref. 6), are used in the numerical solutions. The correlation formulas are valid for temperatures between 1000° and 15,000°K and for pressures between 0.1 and 100 atmospheres.

3.2 NUMBER DENSITIES

The absorption coefficients which are discussed in subsection 3.3, are most conveniently expressed in terms of the gas-particle number densities. The number densities can be easily obtained from the air equation of state if an idealized air chemistry model is adopted. In this model, oxygen dissociation is assumed to begin first as the air temperature is increased. After all the oxygen molecules are dissociated, the nitrogen molecules commence dissociating. When all of the molecules are dissociated, ionization of the atoms begins and no distinction is made between the ionization of the oxygen and nitrogen atoms.

In the current analysis the injected gas is assumed to be inert and no chemical reactions between the ablation products and air are allowed. An examination of the equilibrium composition of nylon phenolic (Fig. 2) shows that the most prominent constituent is carbon monoxide over a wide range of temperatures. The mass fraction equilibrium

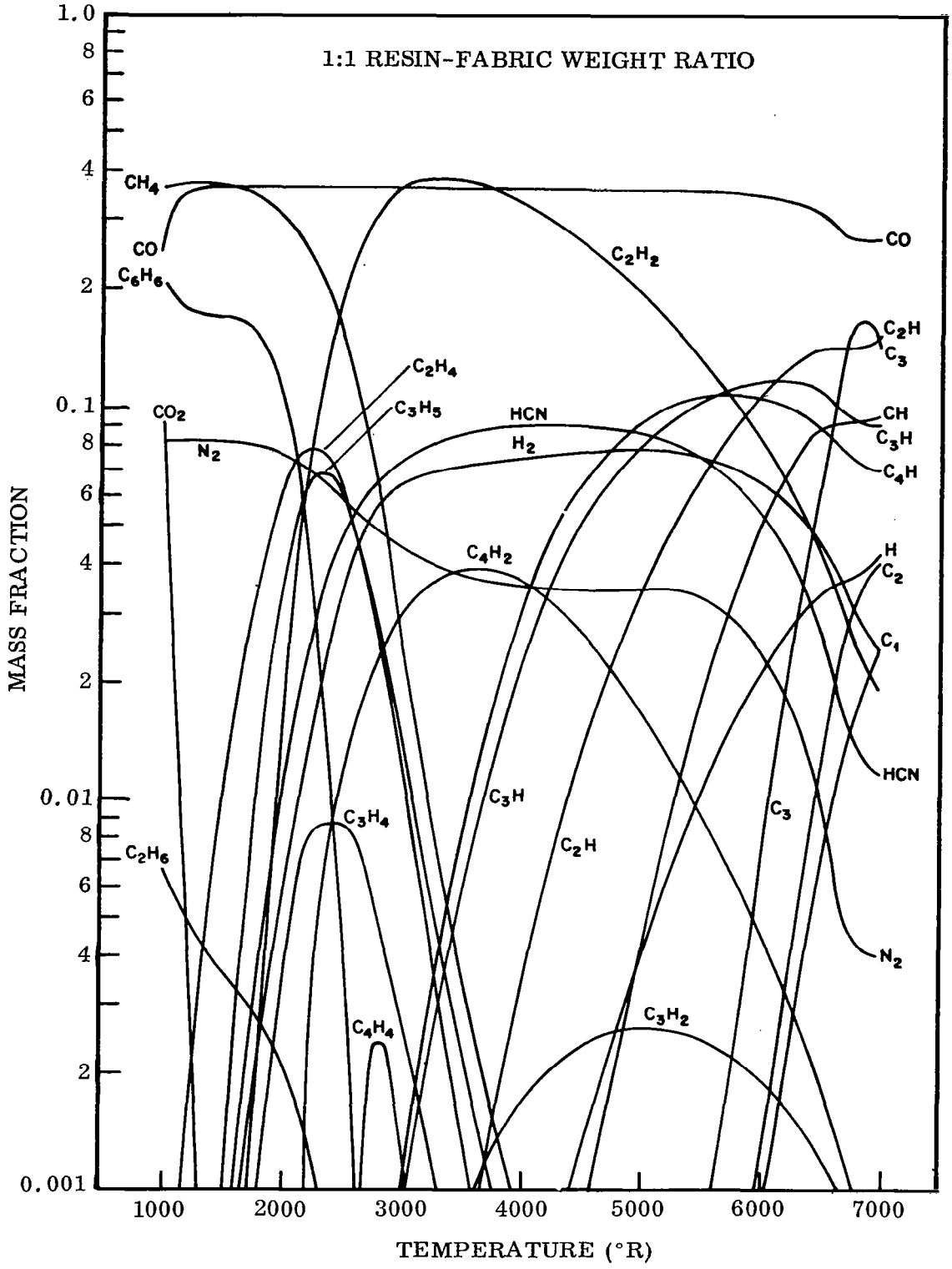

Fig. 2 Equilibrium Composition of the Pyrolysis Products of Nylon-Phenolic (1.0-atm Pressure)

composition curves for refrasil-phenolic and carbon phenolic yield essentially the same result. A further examination of the absorption bands for CO shows that the fourth positive is probably the most important band. Hence, it has been assumed that carbon monoxide is a fixed fraction (mass) of the injected ablation product and only the fourth positive band is considered.

The dissociation of carbon monoxide is accounted for in our simplified model by assuming that the dissociation of CO has the same dependence on the pressure and temperature as N_2 since the dissociation energy of CO and N_2 are somewhat similar (Ref. 7). It is also assumed that the ionization of the carbon atom is identical to the ionization of the oxygen and nitrogen atoms.

The assumption that the thermodynamic properties of the injected gas are identical to air implies that the equation of state and the dissociation and ionization of the two gases have the same dependence on pressure and temperature. However, since CO is the only injected gas considered and its dissociation energy and molecular weight are similar to N_2, the gas model chemistry can be improved by assuming that CO dissociates in the same manner as N_2. This will require a slight empirical adjustment to the number density calculations developed below.

The number density of the molecules, atoms, and ions can be expressed in terms of the total number density and the compressibility Z, by means of the definitions of the total mass and total number density.

$$\rho_t = \rho_m + \rho_a + \rho_i + \rho_e \tag{17}$$

$$N_t = N_m + N_a + N_i + N_e \tag{18}$$

With the equation of state

$$Z = \frac{M_o}{M_t} = \frac{M_o}{RT}\frac{p}{\rho_t} \tag{19}$$

Equation (17) can be rewritten as

$$N_t = N_m \frac{M_m}{M_o} Z + N_a \frac{M_a}{M_o} Z + N_i \frac{M_i}{M_o} Z \tag{20}$$

Now it is necessary to consider particular intervals in the value of the compressibility factor Z in which the gas chemistry is specified. In these intervals, the number densities can be obtained in terms of the total number density and the compressibility factor Z by means of Eqs. (18–20).

Dissociation of Oxygen: $1.0 < Z \leq 1.2$

$$N_{O_2} = N_{t,air}\left(\frac{1.2 - Z}{Z}\right) \tag{21}$$

$$N_O = N_{t,air}\left(\frac{2Z - 2}{Z}\right) \tag{22}$$

$$N_{N_2} = N_{t,air} \frac{0.8}{Z} \tag{23}$$

$$N_{CO} = \alpha_{CO} N_{t,inj} \tag{24}$$

$$N_{t,air} = (1 - C) \frac{Z\rho_t A}{M_o} \tag{25}$$

$$N_{t,inj} = C\frac{\rho_t}{M_o} A \tag{26}$$

Equation (23) states that the number density of N_2 is equal to 0.8 times the total number density of air calculated, assuming no dissociation.

Dissociation of Nitrogen and Carbon Monoxide: $1.2 < Z \leq 2.0$

$$N_O = N_{t,air} \frac{0.4}{Z} \tag{27}$$

$$N_{N_2} = N_{t,\,air}\left(\frac{2 - Z}{Z}\right) \tag{28}$$

$$N_N = N_{t,\,air}\left(\frac{2Z - 2.4}{Z}\right) \tag{29}$$

The total number density of the ablation products is given by

$$N_{t,\,inj} = (1 - \alpha_{CO})\frac{C\rho_t A}{M_o} + \alpha_{CO}\frac{C\rho_t A}{M_o}(Z - 0.2)(0.835 + 0.137Z)$$

$$= N_{t,\,remain} + N_{t,\,CO} \tag{30}$$

where a compressibility dependent correction factor has been applied to the last term, which is the total number density of CO and its products of dissociation, to force CO to dissociate in the same manner as N_2.

$$N_{CO} = N_{t,\,CO}\left[\frac{2 - (Z - 0.2)(0.835 + 0.137Z)}{(Z - 0.2)(0.835 + 0.137Z)}\right] \tag{31}$$

$$N_{C-O} = N_{t,\,CO}\left[\frac{2(Z - 0.2)(0.835 + 0.137Z) - 2}{(Z - 0.2)(0.835 + 0.1372)}\right] \tag{32}$$

Single Ionization of Atoms: $2 < Z \leq 4$

$$N_o = 0.2\,(1 - C)\,N_t\left(\frac{4 - Z}{Z}\right) \tag{33}$$

$$N_N = 0.8\,(1 - C)\,N_t\left(\frac{4 - Z}{Z}\right) \tag{34}$$

$$N_{C-O} = \alpha_{CO}\,C\,N_t\left(\frac{4 - Z}{Z}\right) \tag{35}$$

$$N_i = N_t\left(\frac{Z - 2}{Z}\right) \tag{36}$$

$$N_t = \frac{Z\rho_t A}{M_o} \tag{37}$$

Double Ionization of Atoms: $4 < Z \leq 6$

$$N_i = N_t\left(\frac{6}{Z} - 1\right) \tag{38}$$

$$N_{ii} = N_t\left(1 - \frac{4}{Z}\right) \tag{39}$$

3.3 ABSORPTION COEFFICIENTS

The radiative energy transfer within the shock layer depends critically on the absorption coefficient of the gas particles. The absorption coefficient is dependent on the nature of the gas particle, its number density, the gas temperature, and the radiation frequency. The absorption coefficients utilized in the present analysis are summarized in Fig. 3. An examination of the molecular absorption coefficients for air given in Refs. 8, 9, and 10 shows that the only important air molecular absorption coefficients are the O_2 Schumann-Runge continuum and the N_2 Birge-Hopfield band. For typical ablators such as nylon phenolic and carbon phenolic, the most important contribution to the gas mixture absorption coefficient appears to be the CO fourth positive band. This is the only injected gas absorption band accounted for in this analysis. Other molecules, such as CN and C_2, either have effective absorption cross sections ($\sigma^* = \kappa_\nu/N$) which are too small or the number density of the molecule is not large enough for the molecule to contribute significantly to the optical depth of the gas mixture.

All of the important absorption coefficients summarized in Fig. 3 are given by simple analytical expressions in terms of the particle number density, temperature, and the radiation frequency. The equations are used to evaluate the radiation flux gradient term in the energy equation to obtain numerical solutions.

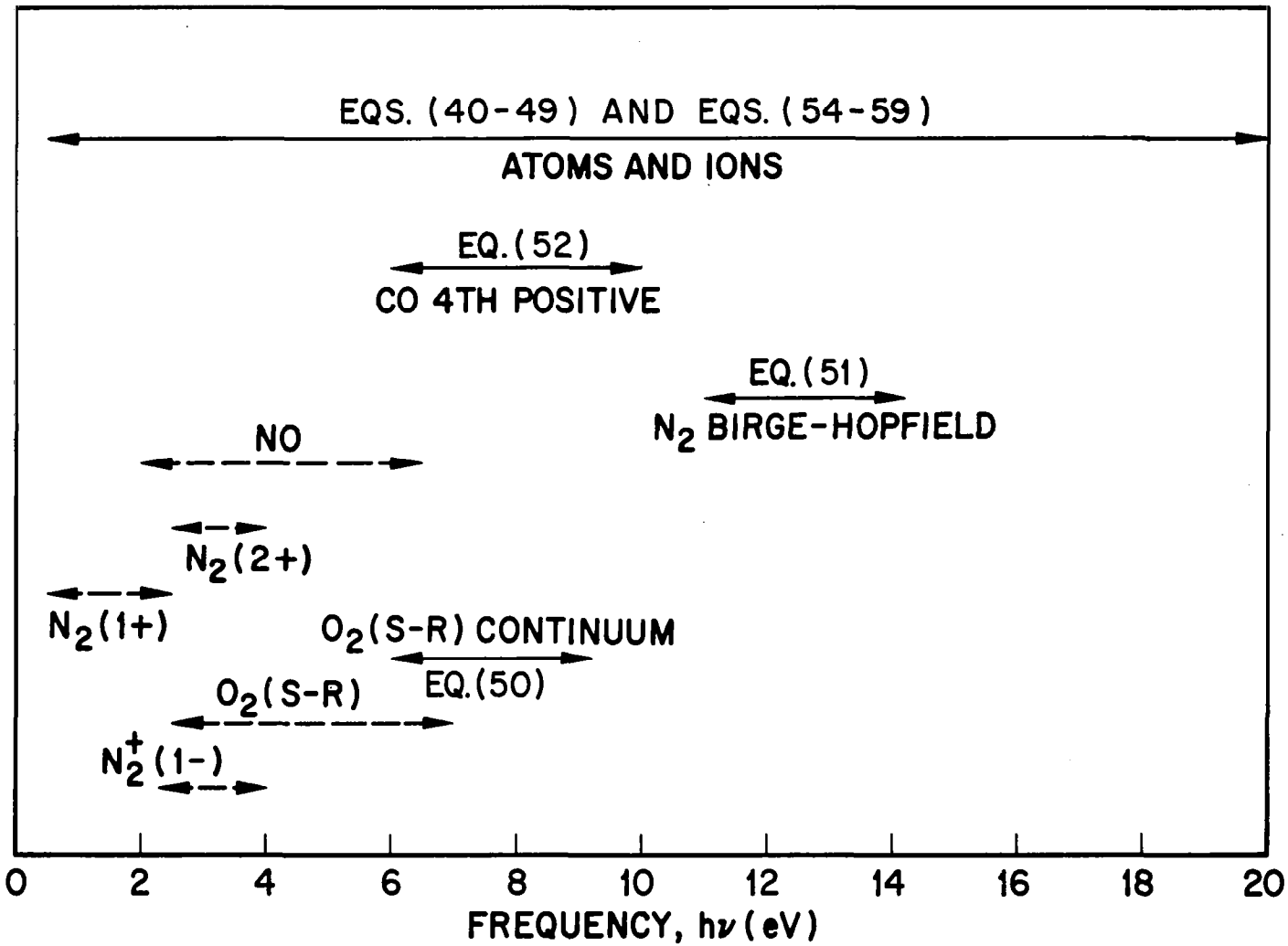

Fig. 3 Summary of Absorption Coefficients

The continuum absorption coefficients due to bound-free and free-free transitions for the neutral and singly ionized atoms of nitrogen and oxygen were obtained from the theory of Biberman (Ref. 11) and Armstrong et al (Ref. 12, 13). Biberman's results are used for the free-free and bound-free transitions from the higher excited states while Armstrong's detailed quantum-mechanical calculations are used to provide cross-sections for photon absorption due to transitions from the ground and low lying excited states.

The absorption coefficient for air is written as the sum of the individual species absorption coefficients

$$\kappa_\nu(\chi) = [1 - e^{-\chi}]\,[(\kappa_\nu)_N + (\kappa_\nu)_O + (\kappa_\nu)_i]$$

where the term in the first bracket accounts for induced emission. The absorption coefficient of the oxygen ion is assumed to be equal to that of the nitrogen ion. This approximation is acceptable since the ions contribute little to the total absorption coefficient except at the higher frequencies where the radiation from the shock layer gas is likely to be black body.

The absorption coefficients for the various species are listed below for the indicated frequency intervals.

$0 \leq h_\nu \leq 4.22$

$$(\kappa_\nu)_N = 4.5\ \tilde{a}\ N_N\ \theta\ e^{-(\chi_N - \chi)}\ \frac{\xi_N}{(h\nu)^3} \tag{40}$$

$$(\kappa_\nu)_O = \frac{8}{9}\ \tilde{a}\ N_O\ \theta\ e^{-(\chi_O - \chi)}\ \frac{\xi_O}{(h\nu)^3} \tag{41}$$

$$(\kappa_\nu)_i = 1.33\ \tilde{a}\ N_i\ \theta\ e^{-(\chi_i - \chi)}\ \frac{\xi_i}{(h\nu)^3} \tag{42}$$

where

$$\tilde{a} = 7.25 \times 10^{16}\ \mathrm{cm}^2\text{-ev}^2$$

$$\chi_N = 14.3/\theta\ ,\ \chi_O = 13.4/\theta\ ,\ \chi_i = 25.5/\theta$$

$$\chi = h\nu/kT = h\nu/\theta$$

ξ_N , ξ_O , ξ_i = quantum-mechanical correction factor (Fig. 4)

$4.22 \leq h\nu \leq 10.8$

$$(\kappa_\nu)_N = [\text{Eq. (40)}]\ e^{(4.22/\theta - \chi)} \tag{43}$$

$$(\kappa_\nu)_O = [\text{Eq. (41)}]\ e^{(4.22/\theta - \chi)} \tag{44}$$

$$(\kappa_\nu)_i = [\text{Eq. (42)}]$$

$10.8 \leq h\nu \leq 12.0$

$$(\kappa_\nu)_N = [\text{Eq. (43)}] + N_N \cdot \varphi_{N,1} \tag{45}$$

$$(\kappa_\nu)_O = [\text{Eq. (44)}]$$

$$(\kappa_\nu)_i = [\text{Eq. (42)}]\ e^{(11.2/\theta - \chi)} \tag{46}$$

$12 < h\nu \leq 13.4$

$$(\kappa_\nu)_N = [\text{Eq. (43)}] + N_N (\varphi_{N,1} + \varphi_{N,2}) \tag{47}$$

$$(\kappa_\nu)_O = [\text{Eq. (44)}]$$

$$(\kappa_\nu)_i = [\text{Eq. (46)}]$$

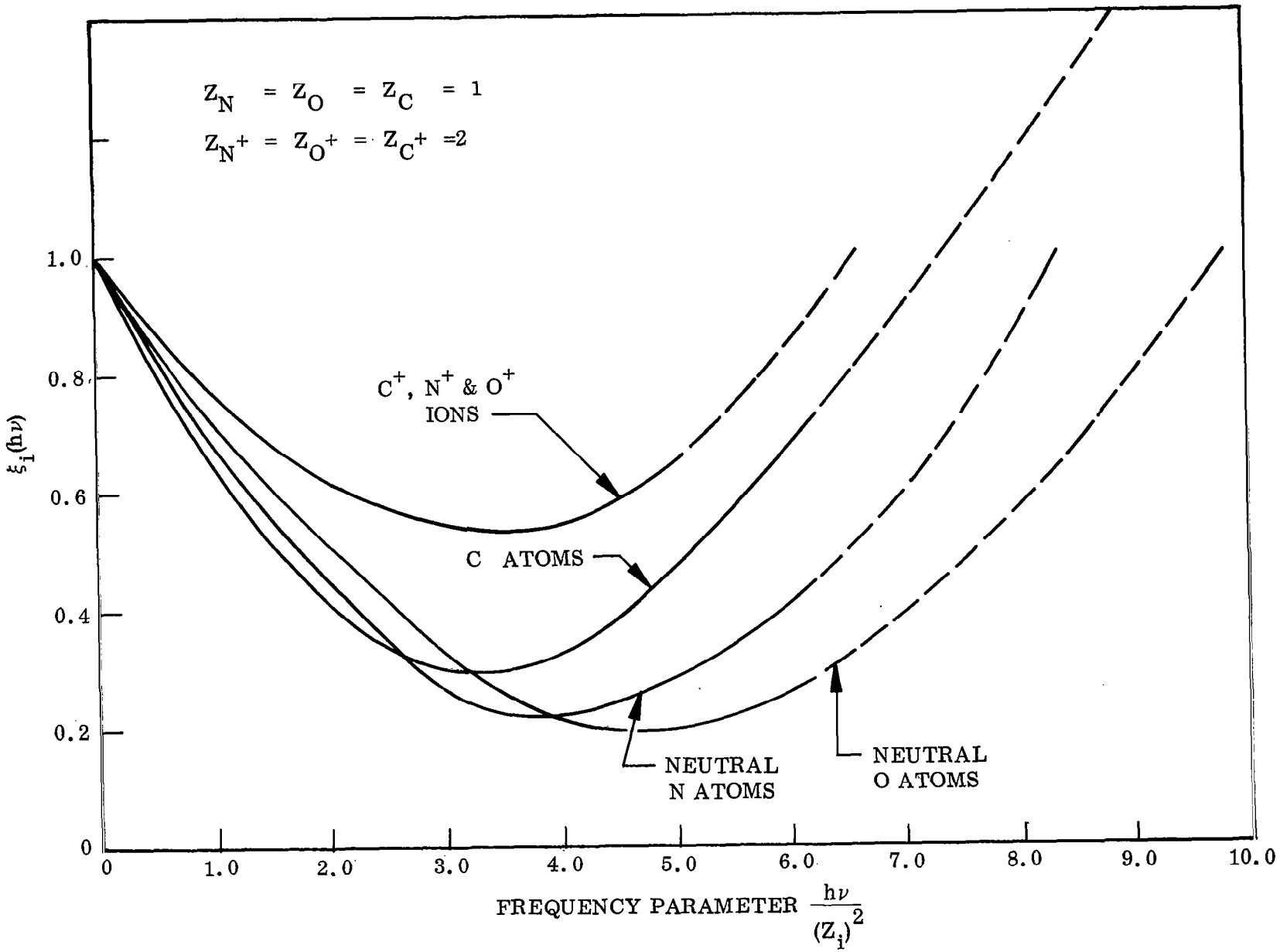

Fig. 4 Quantum-Mechanical Correction Factor $\xi(h\nu)$

$13.4 < h\nu \leq 14.3$

$$
\begin{aligned}
(\kappa_\nu)_N &= [\text{Eq. (47)}] \\
(\kappa_\nu)_O &= [\text{Eq. (44)}] + N_O \cdot \varphi_{O,1} \qquad (48) \\
(\kappa_\nu)i &= [\text{Eq. (46)}
\end{aligned}
$$

$14.3 < h\nu \leq 20$

$$
\begin{aligned}
(\kappa_\nu)_N &= [\text{Eq. (43)}] + N_N (\varphi_{N,1} + \varphi_{N,2} + \varphi_{N,3}) \qquad (49) \\
(\kappa_\nu)_O &= [\text{Eq. (48)}] \\
(\kappa_\nu)_i &= [\text{Eq. (46)}]
\end{aligned}
$$

where

$$
\varphi_{N,1} = 5.16 \times 10^{-17} \frac{e^{-(\chi_N - 10.8/\theta)}}{\left[4 + 10e^{-(2.38/\theta)} + 6e^{-(3.57/\theta)}\right]}
$$

$$
\varphi_{N,2} = 6.4 \times 10^{-17} \frac{e^{-(\chi_N - 12/\theta)}}{\left[4 + 10e^{-(2.38/\theta)} + 6e^{-(3.57/\theta)}\right]}
$$

$$
\varphi_{N,3} = 3.16 \times 10^{-17} \frac{1}{\left[4 + 10e^{-(2.38/\theta)} + 6e^{-(3.57/\theta)}\right]}
$$

$$
\varphi_{O,1} = 3.6 \times 10^{-17} \frac{1}{\left[9 + 5e^{-(1.98/\theta)} + e^{-(4.18/\theta)}\right]}
$$

A comparison of the absorption coefficient as predicted by Eqs. (40) – (49) with the numerical results of Armstrong is shown in Fig. 5. The agreement is highly satisfactory.

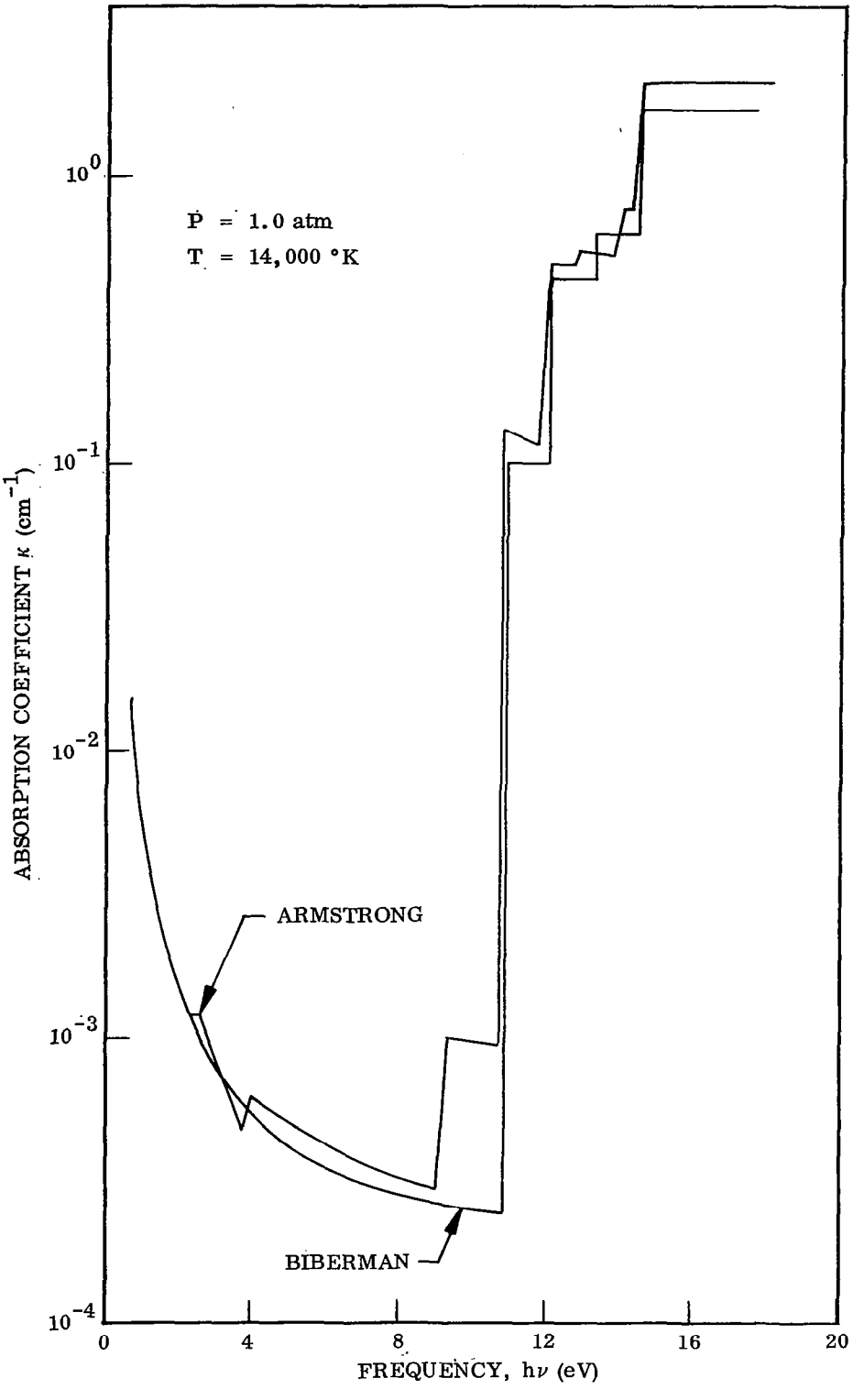

Fig. 5 Comparison of Biberman and Armstrong Continuum Absorption Coefficients for Air

The absorption coefficients for molecular oxygen Schumann-Runge continuum were obtained from the results of Evans and Schexnayder (Ref. 9). In Ref. 9 the authors discuss the approximate formula of Sulzer-Wieland and point out its deficiency at elevated temperatures ($T \approx 10,000°K$). At lower temperatures where the molecular oxygen is present in a gas mixture in chemical equilibrium, the approximate results of Sulzer-Wieland given below are adequate for present purposes.

$$\kappa_\nu = 1.49 \times 10^{-17} N_{O_2} \left[\tanh\left(\frac{0.0975}{\theta}\right)\right]^{1/2} \exp\left[-\tanh\left(\frac{0.0975}{\theta}\right) \times \left(\frac{h\nu - 8.56}{0.805}\right)^2\right] \tag{50}$$

The absorption coefficient for the nitrogen Birge-Hopfield band was obtained from results of R. Allen (Ref. 10). The cross section for $T = 7000°K$ was approximated and used to obtain the following expression for the absorption coefficient.

$$\kappa_\nu = 1.2 \times 10^{-17} N_{N_2} \exp\left[-\left|h\nu - 13.6 + \left(1 - \frac{0.603}{\theta}\right)\right|^{1.3}\right] \tag{51}$$

Franck-Condon factors calculated by Nichols (Ref. 14) were employed by Nicolet (Ref. 15) to calculate the absorption coefficient for the CO fourth positive band. The f-number was assumed to be 0.15 (Ref. 16). A much smaller value for the f-number has been reported in the literature (Ref. 17). However, the larger value is used in the numerical solutions to examine the maximum effect of absorption by the ablation products.

$$\kappa_\nu = N_{CO} \frac{1.8 \times 10^3 f}{L} e^{-|h\nu - 8.25|^2} \tag{52}$$

The effective cross sections, defined by

$$\sigma^* = \frac{\kappa_\nu}{N} \tag{53}$$

for the three molecules discussed above are presented in Fig. 6.

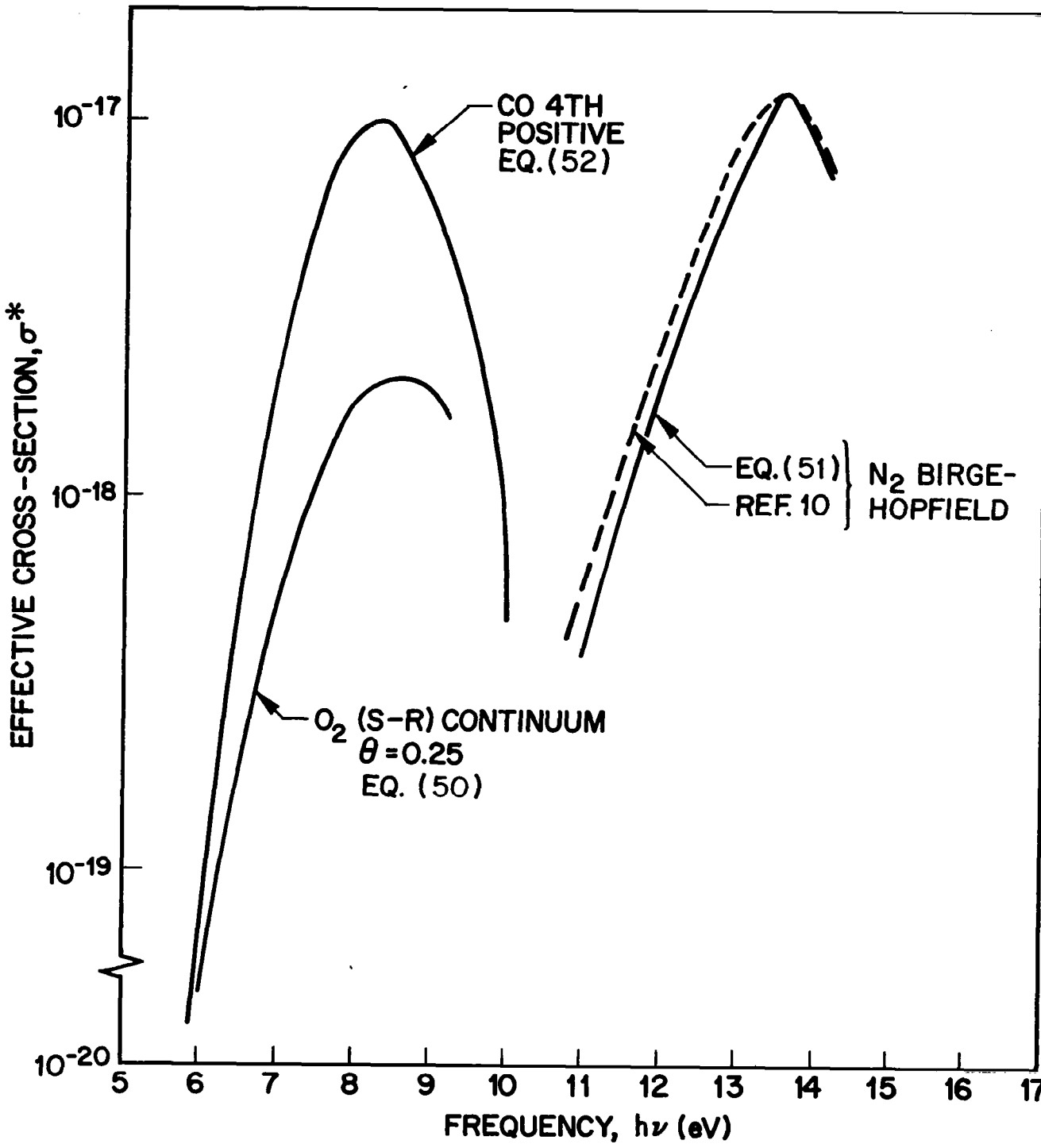

Fig. 6 Effective Cross Section of Molecules

The continuum absorption coefficients for neutral carbon atoms were determined from a method similar to that used for nitrogen and oxygen atoms. Biberman's theory was used to calculate the free-free contribution and the free-bound contributions from the higher excited states. Photoionization cross-sections resulting from detailed quantum-mechanical calculations were available for the low lying excited states, Ref. (18), and ground state, Ref. (19). The absorption coefficients for various frequency intervals are listed below.

$0 \leq h\nu \leq 3.78$

$$(\kappa_\nu)_C = 1.33\ \tilde{a}\ \frac{N_{C-O}}{2}\ \theta\ e^{-(\chi_C - \chi)}\ \frac{\xi_C}{(h\nu)^3} \tag{54}$$

$3.78 \leq h\nu \leq 7.08$

$$(\kappa_\nu)_C = 1.33\ \tilde{a}\ \frac{N_{C-O}}{2}\ \theta\ e^{-(\chi_C - 3.78/\theta)}\ \frac{\xi_C}{(h\nu)^3} \tag{55}$$

$7.08 \leq h\nu \leq 8.51$

$$(\kappa_\nu)_C = [\text{Eq. (54)}] + \frac{N_{C-O}}{2} \cdot \varphi_{C,1} \tag{56}$$

$8.51 \leq h\nu \leq 10$

$$(\kappa_\nu)_C = [\text{Eq. (54)}] + \frac{N_{C-O}}{2} (\varphi_{C,1} + \varphi_{C,2}) \tag{57}$$

$10 \leq h\nu \leq 11.26$

$$(\kappa_\nu)_C = [\text{Eq. (54)}] + \frac{N_{C-O}}{2} (\varphi_{C,1} + \varphi_{C,2} + \varphi_{C,3}) \tag{58}$$

$h\nu > 11.26$

$$(k_\nu)_C = [\text{Eq. (54)}] + \frac{N_{C-O}}{2}(\varphi_{C,1} + \varphi_{C,2} + \varphi_{C,3} + \varphi_{C,4}) \tag{59}$$

where

$$\chi_C = 11.26/\theta$$

$$\xi_C = \text{quantum-mechanical correction factor (Fig. 5)}$$

$$\varphi_{C,1} = 5 \times 10^{-17} \frac{e^{-(\chi_C - 7.08/\theta)}}{\Sigma_C}$$

$$\varphi_{C,2} = 2.2 \times 10^{-17} \frac{e^{-(\chi_C - 8.51/\theta)}}{\Sigma_C}$$

$$\varphi_{C,3} = 8.5 \times 10^{-17} \frac{e^{-(\chi_C - 10/\theta)}}{\Sigma_C}$$

$$\varphi_{C,4} = 9.9 \times 10^{-17} \frac{1}{\Sigma_C}$$

$$\Sigma_C = 9 + e^{-2.68/\theta} + 5(e^{-1.265/\theta} + e^{-4.18/\theta})$$

Section 4
NUMERICAL METHOD

The first step in the numerical method of solution is to obtain a solution at the stagnation point. The integrated momentum and species continuity equations, Eqs. (7) and (8), are first multiplied by u_δ. Since $u_\delta = 0$ at the stagnation point, the derivatives $dI_1/d\xi$ and $dI_2/d\xi$ are eliminated and the equations reduce to algebraic equations. These two equations along with the equations which define the a_i's, c_i's, I_1, I_2, and δ can be solved by iterations provided the shock curvature $d\phi/d\xi$ is known. With an initial guess for the shock curvature, the momentum and species continuity equations can be solved in conjunction with the energy equation. In the species continuity equation, Eq. (8), the quantity $(\rho\mu)_{\delta_c}$ was approximated by $(\rho\mu)_\delta$. For the mass injection rates considered, the error introduced by this approximation is of the order of a few percent. In the energy equation, the radiative flux is evaluated at approximately 20 frequency points. The integration over frequency is then performed numerically.

The solution downstream of the stagnation point proceeds in a similar manner except that the streamwise derivatives are evaluated by means of Eq. (13). For the first iteration, the shock detachment distance is calculated from the assumed shock curvature variation and the stagnation-point standoff distance given by the stagnation-point solution.

The flow field calculated in this manner is then used to calculate a new shock shape which then forms the basis of the next iteration.

Section 5
DISCUSSION OF RESULTS

5.1 COMPARISON OF PRESENT RESULTS TO PREVIOUS SOLUTIONS

To establish the validity of the present results, a comparison is made with other existing solutions wherever possible. In Fig. 7, the stagnation-point heat-transfer rates obtained from the present solution for a nonradiating shock layer are compared with boundary-layer theory (Ref. 20). It is seen that the agreement is quite satisfactory. The slight discrepancies are believed to be caused by the inability of the velocity profiles obtained from the integral solution to accurately represent the thinning out of the viscous layer as the Reynolds number is increased.

In Fig. 8, stagnation-point velocity, enthalpy, and concentration profiles are compared with the numerical results of Howe (Ref. 21). These profiles include the effect of mass injection and radiation. In the present analysis, the radiation is evaluated for nongray gas, whereas Howe makes use of the gray-gas approximation. For these flight conditions, the manner in which the radiative transport is treated does not have a significant effect on the profiles and one can meaningfully compare the results. Whether or not the gray-gas approximation is employed will, however, have a significant effect on the radiative flux to the wall. The profiles are seen to be generally in good agreement. The convective heat transfer is also in good agreement, as demonstrated in Fig. 9 which shows the effect of mass injection on convective heating. The present results predict a somewhat smaller reduction in convective heating by mass injection than the correlation equation of Howe. Note the small effect of radiation cooling on the reduction of the convective heating by mass injection.

5.2 EFFECT OF SELF-ABSORPTION ON TOTAL HEATING

From previous work, it was expected that self-absorption would decrease the radiative flux to the surface by a significant amount. This naturally raises the question, "How

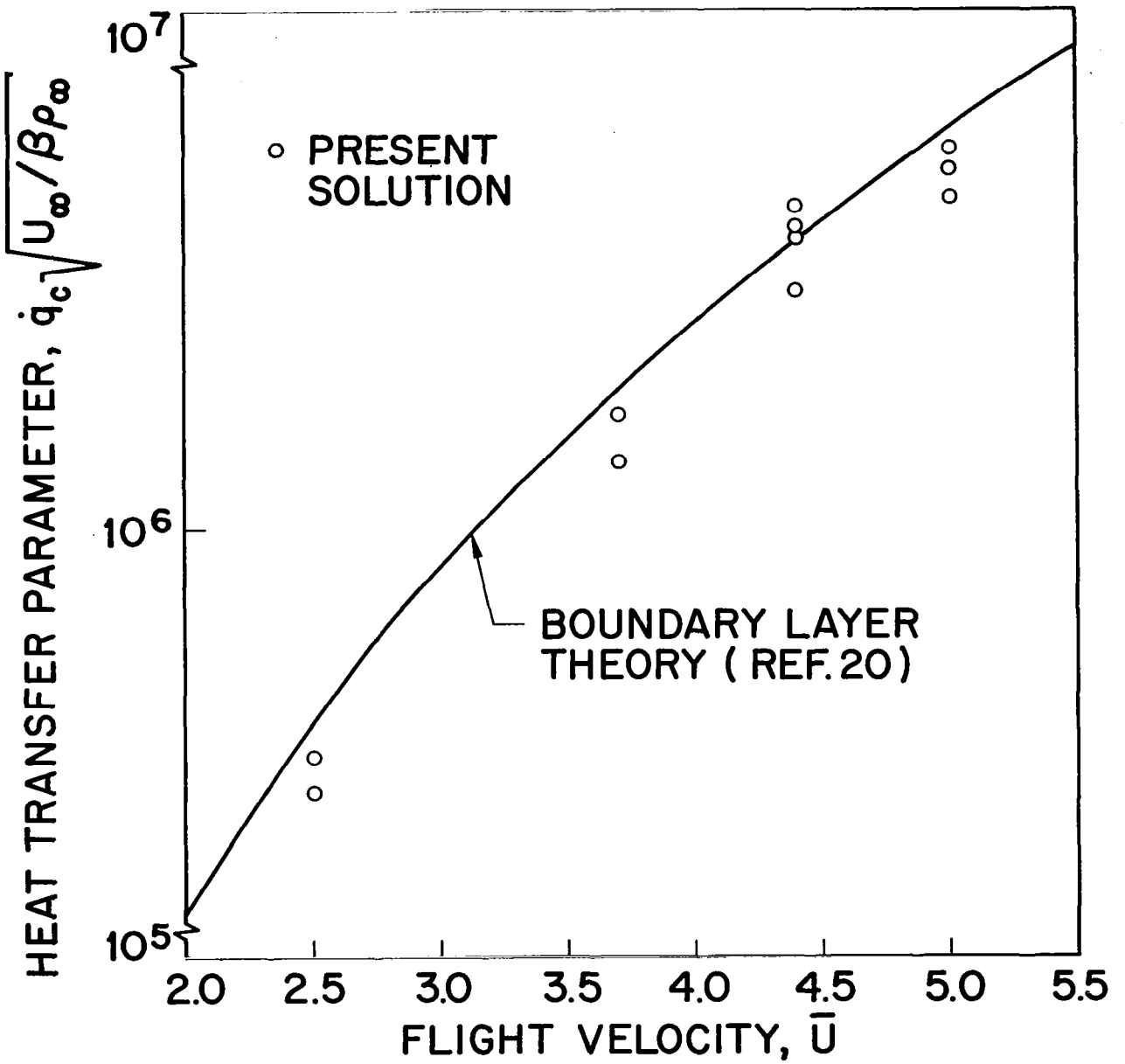

Fig. 7 Comparison of Stagnation-Point Heat-Transfer Results

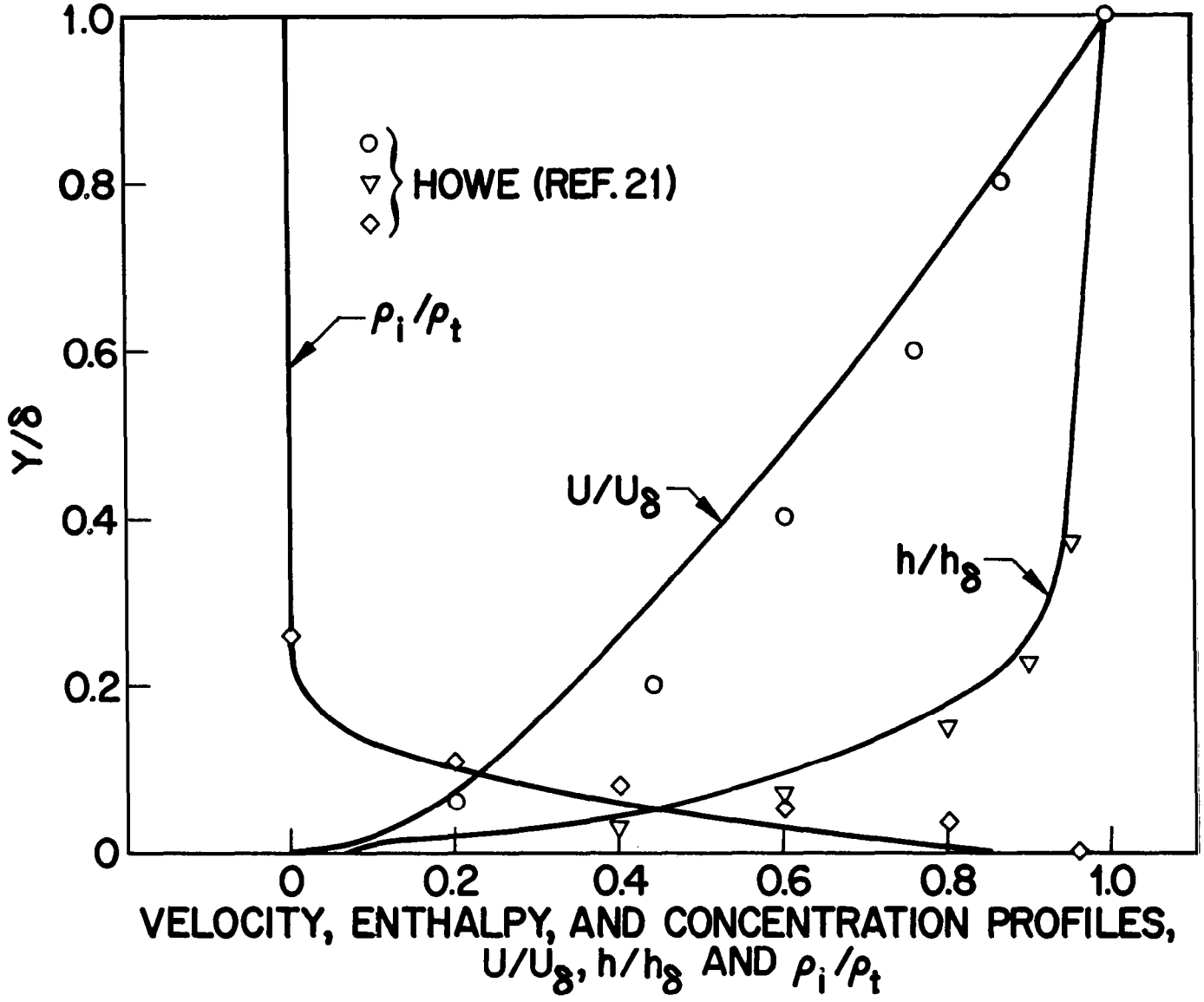

Fig. 8 Stagnation Point Velocity, Enthalpy, and Concentration Profiles, U = 4.1, P_δ = 1 atm, R = 1 ft, $(\rho\nu)/(\rho U)_\infty$ = 0.053

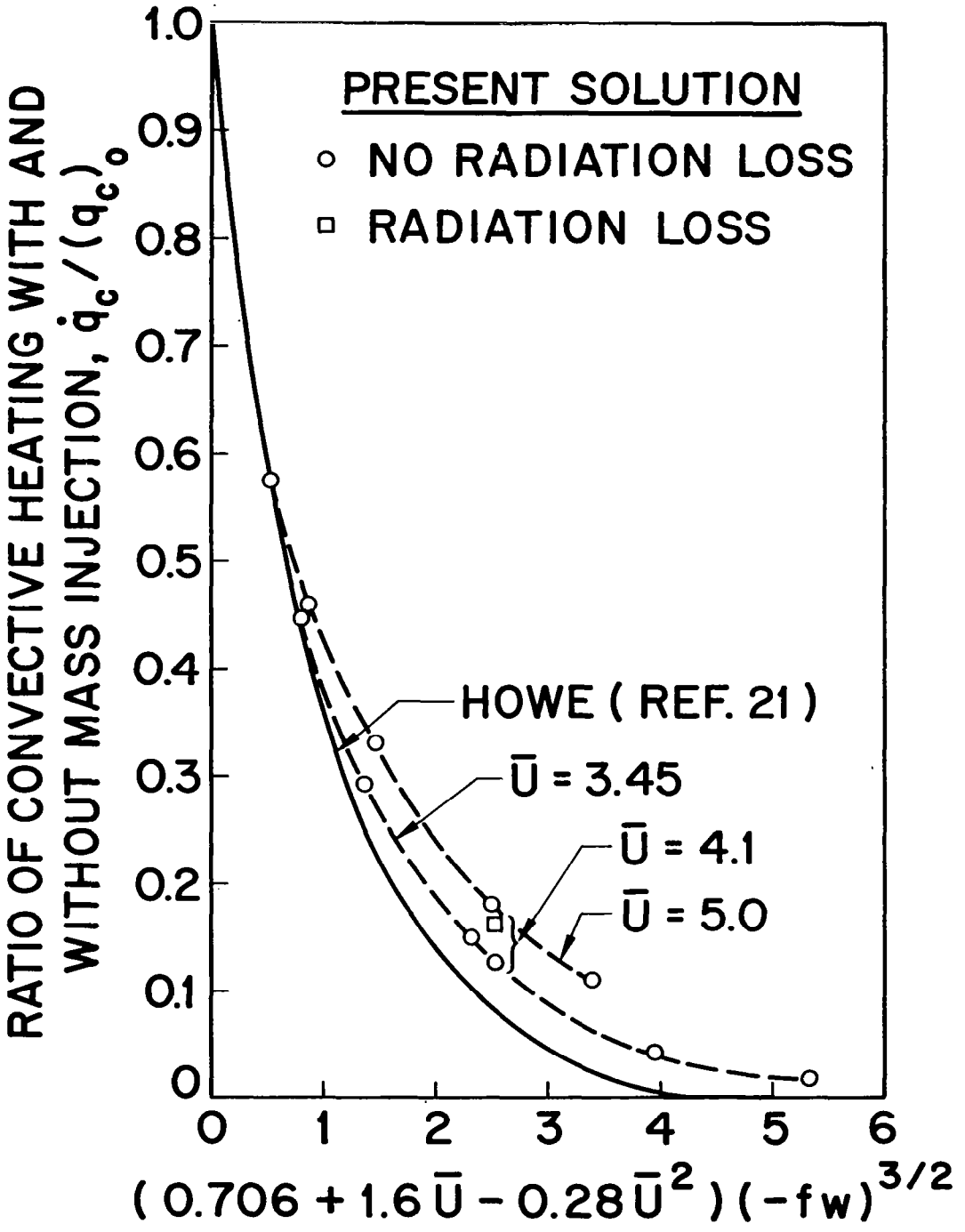

Fig. 9 Reduction of Convective Heating Due to Mass Injection

is the convective heating affected by this absorption of radiant energy in the shock layer?" To answer this question, numerous stagnation-point solutions were obtained. Solutions were obtained for an optically thin gas without radiation loss, a non-gray gas with radiation loss without molecular absorption, and a non-gray gas with radiation loss with molecular absorption. The effect of mass injection was also included. The convective, radiative, and total heat-transfer rates are presented graphically in Fig. 10 and summarized in Table 1.

We note generally that the combined effect of radiation loss and self-absorption reduces the radiative heating significantly but has a small effect on the convective heating. Self-absorption and radiation loss both tend to decrease the radiative flux to the surface. On the other hand, radiation loss tends to decrease the convective heating, while self-absorption has a compensating effect in that it tends to increase the convective heating. Comparison of results with and without molecular absorption shows that the convective heating is slightly increased by radiative absorption by molecules in the viscous layer, while the radiative heating is slightly decreased. The net effect of self-absorption by all the gas particles in the shock layer is to cause a substantial decrease in the total heating due primarily to the reduction in the radiative heating. This implies that a large fraction of the radiant energy is "trapped" in the shock layer gas.

In Fig. 11, the monochromatic heat flux is presented for one flight condition for both an optically thin gas without radiation loss and for a non-gray gas with radiation loss. These results also include the effect of mass injection. The effect of self-absorption is seen to be primarily in the ultraviolet portion of the spectrum. The increase in the monochromatic flux at a frequency of 8.25 eV is due to the CO fourth positive band. Similar results for a higher flight velocity are presented in Fig. 12. In this case the number density of CO was not large enough to cause any variation in the monochromatic flux as was the case in the previous results. Note that at the ground excited state ionization edge where the absorption coefficient is increased discontinuously, the monochromatic flux increases for the optically thin case but decreases for the non-gray case. This behavior for the non-gray case is due to the non-isothermal structure of the shock layer. A step increase in the absorption coefficient causes the gas to emit as a black body at a lower temperature at frequencies greater than the location of the ground excited state ionization edge.

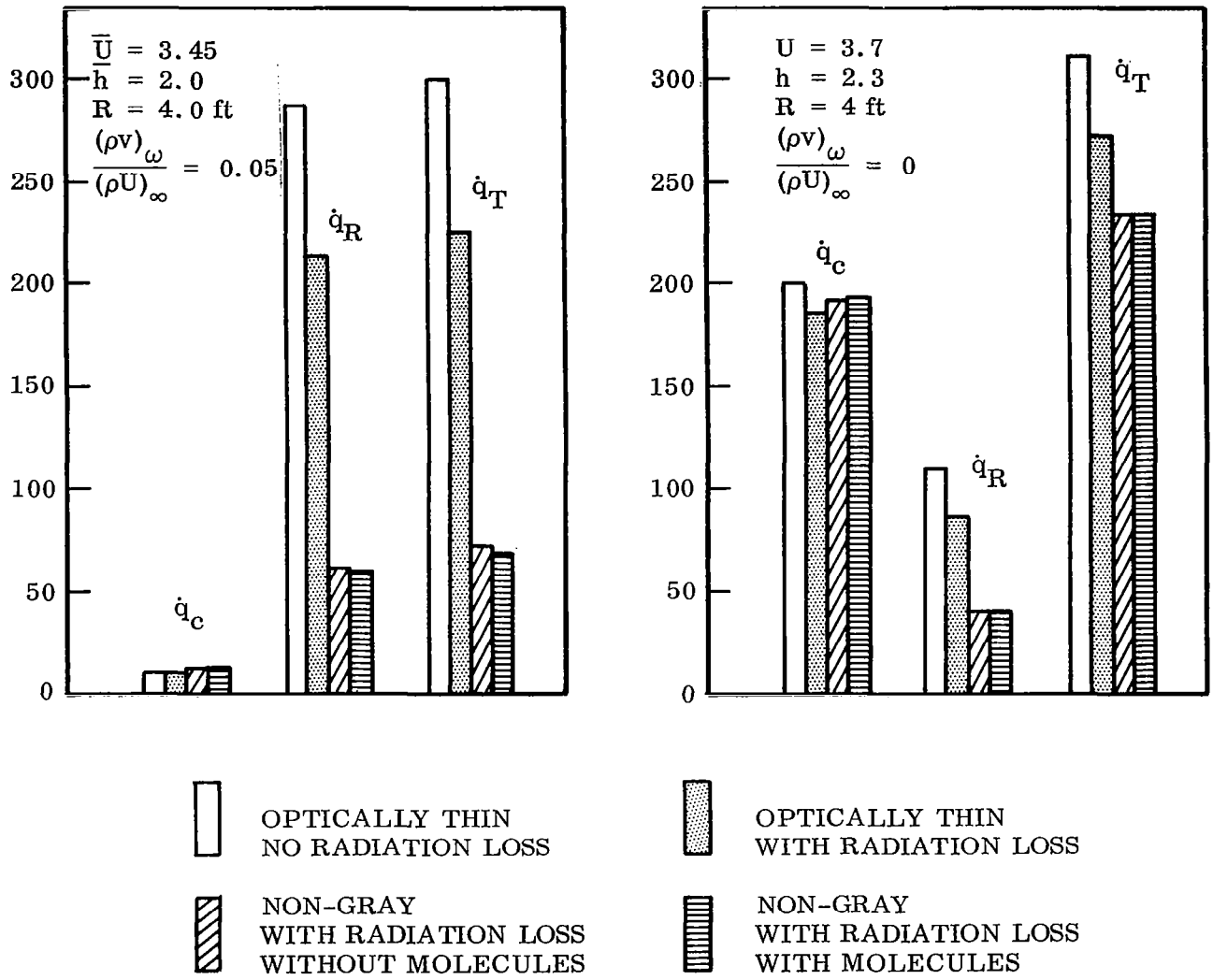

Fig. 10 Summary of Stagnation Point Convective and Radiative Heat Transfer

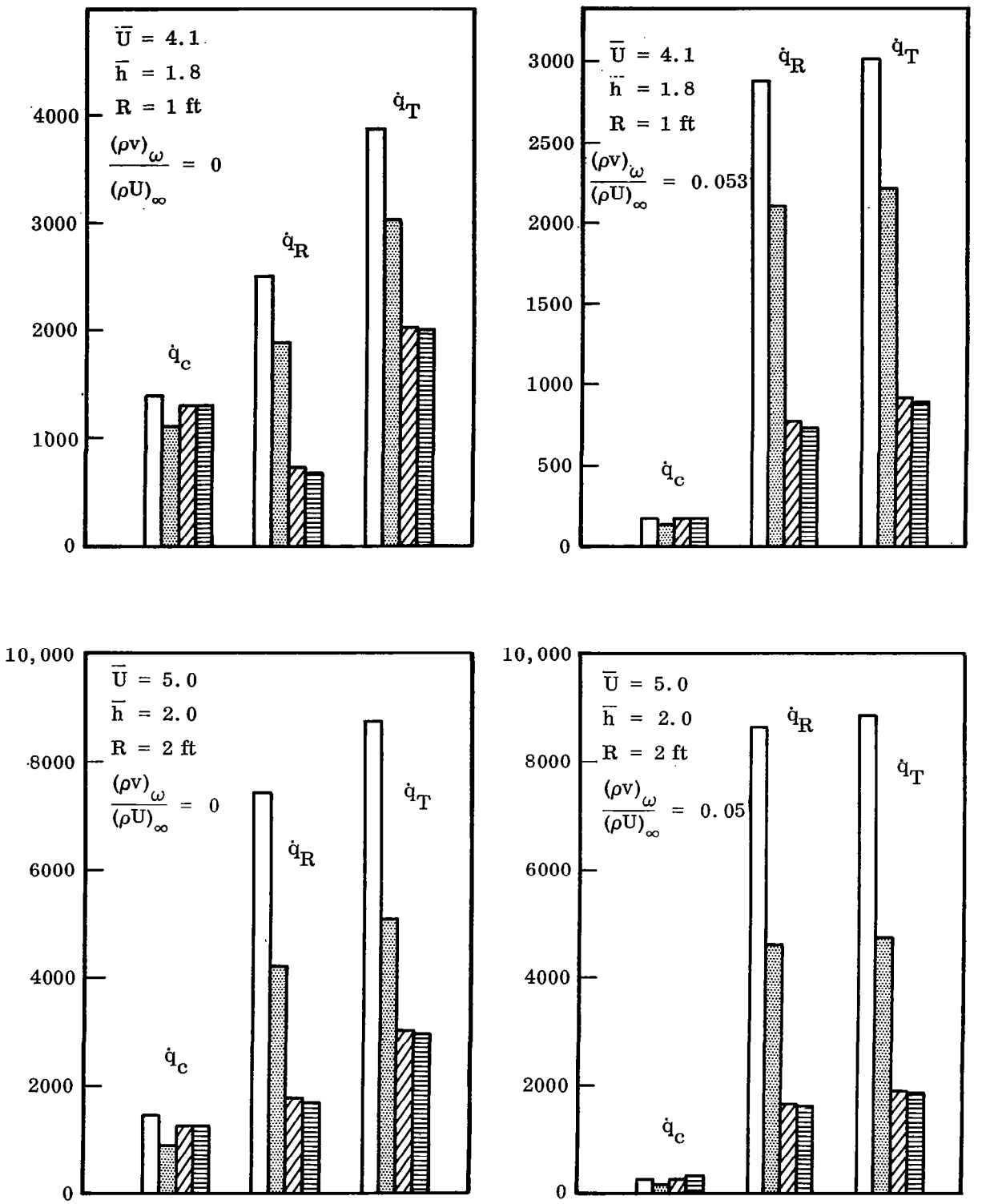

Fig. 10 Summary of Stagnation Point Convective and Radiative Heat Transfer (cont.)

Table 1

SUMMARY OF CONVECTIVE AND RADIATIVE HEAT TRANSFER

$\bar{U}$	$\bar{h}$	R (ft)	$\frac{(\rho v)_w}{(\rho U)_\infty}$	Optically Thin, No Radiation Loss			Optically Thin, With Radiation Loss			Non-gray, With Radiation Loss, Without Molecules			Non-gray, With Radiation Loss, With Molecules		
				$\dot{q}_C$ (a)	$\dot{q}_R$	$\dot{q}_T$	$\dot{q}_C$	$\dot{q}_R$	$\dot{q}_T$	$\dot{q}_C$	$\dot{q}_R$	$\dot{q}_T$	$\dot{q}_C$	$\dot{q}_R$	$\dot{q}_T$
3.45	2.0	4	0.05	10	288	298	9.3	216	225.3	10.3	61	71.3	10.5	58	68.5
3.7	2.3	4	0	199	109	308	185	86.6	271.6	193	40	233	194	40	234
4.1	1.8	1	0	1382	2500	3882	1130	1875	3005	1305	715	2020	1315	680	1995
4.1	1.8	1	0.053	173	2880	3053	136	2090	2226	162	760	922	170	724	894
5.0	2.0	2	0	1420	7450	8870	873	4200	5075	1255	1750	3005	1260	1680	2940
5.0	2.0	2	0.05	242	8650	8892	125.5	4600	4725.5	231	1668	1899	256	1605	1861

(a) $\dot{q}_C$, $\dot{q}_R$, $\dot{q}_T$, Btu/ft^2-sec.

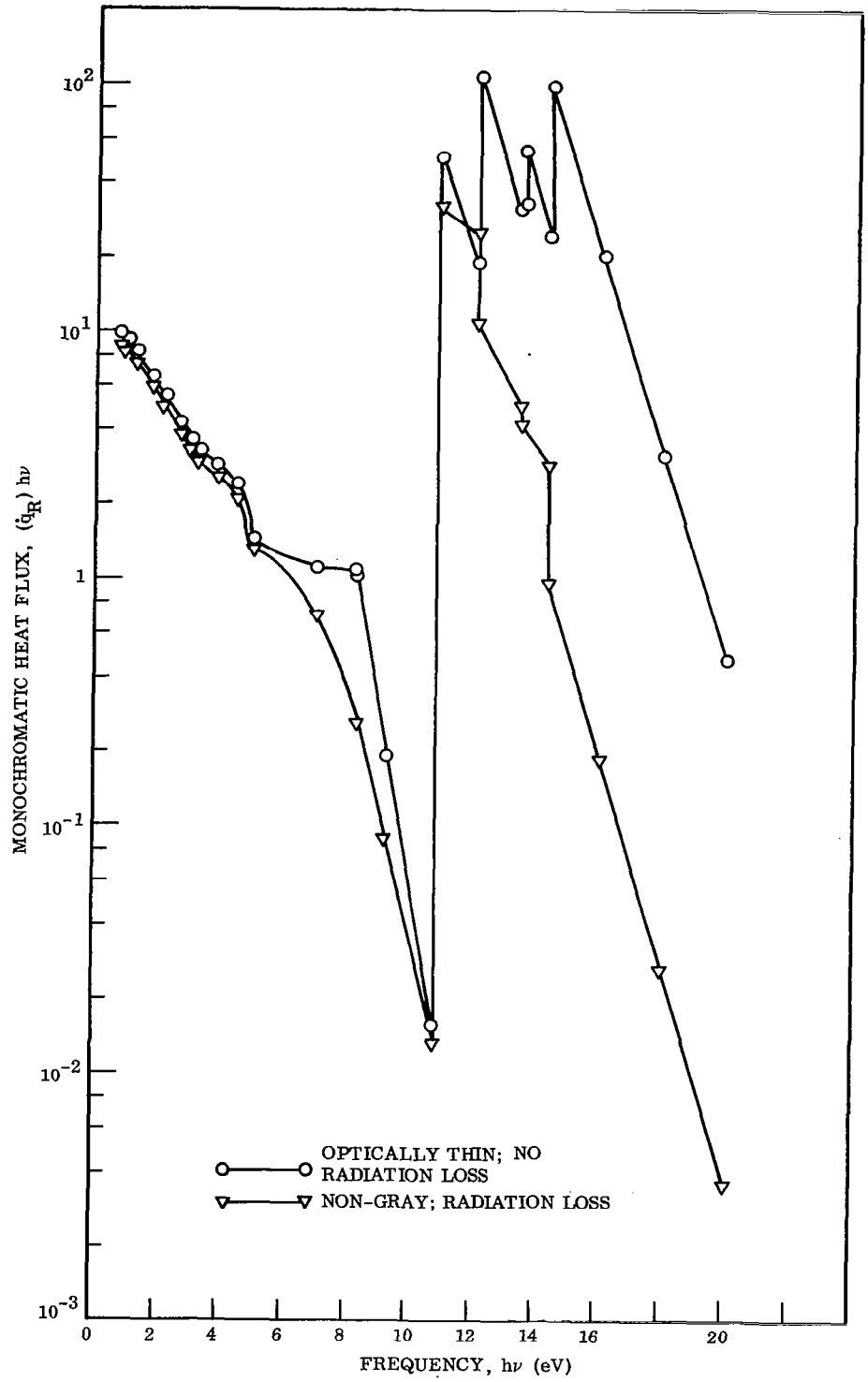

Fig. 11 Monochromatic Heat Flux, $\bar{U} = 3.45$, $\bar{h} = 2.0$, R = 4 ft, With Mass Injection, $(\rho v)_w/(\rho U)_\infty = 0.05$

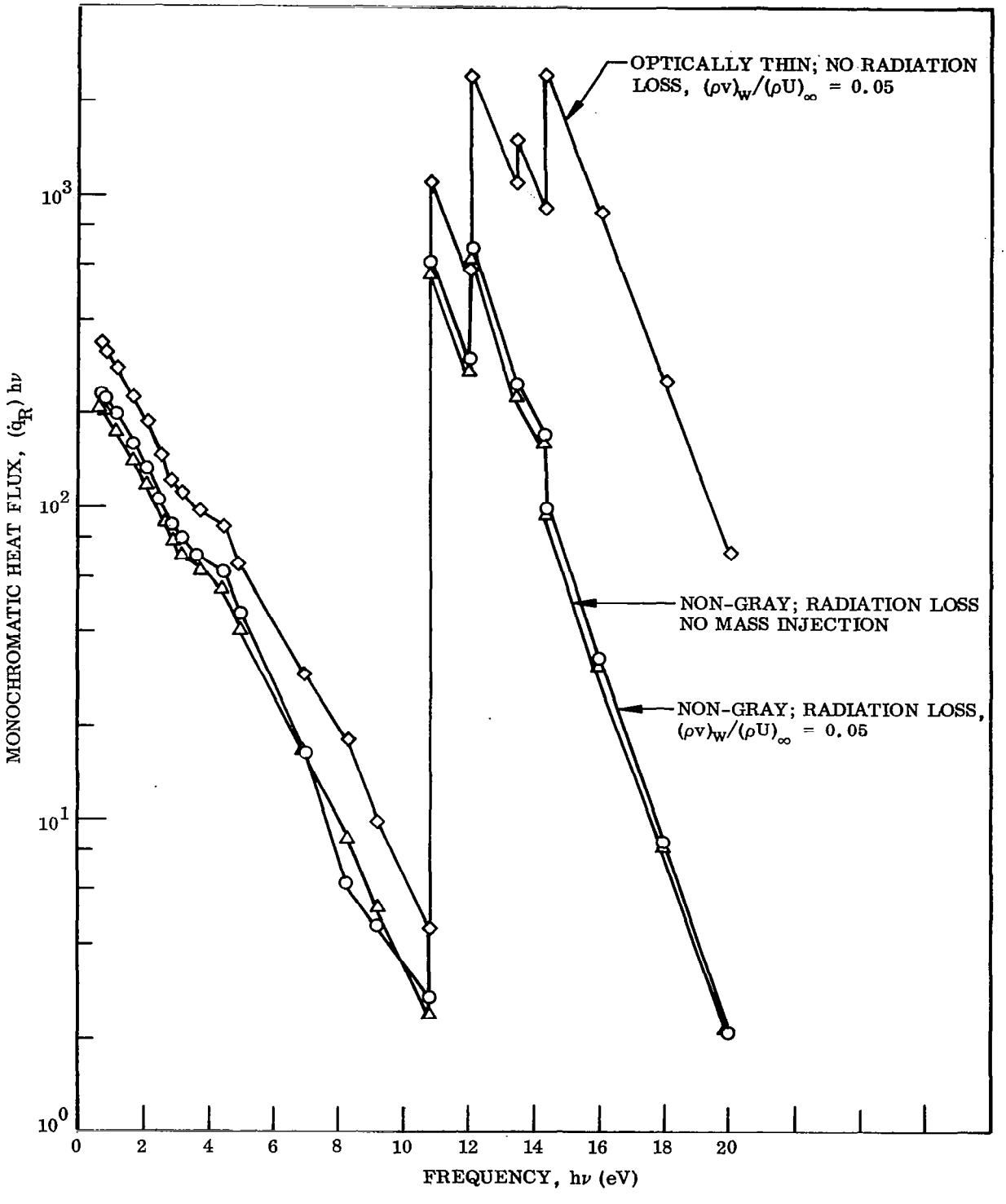

Fig. 12 Monochromatic Heat Flux, $\bar{U} = 5.0$, $\bar{h} = 2.0$, R = 2 ft

5.3 EFFECT OF SELF-ABSORPTION ON NOSE RADIUS FOR MINIMUM TOTAL HEATING

Since self-absorption decreases the total heating, it would be expected to have a significant effect on the nose radius which results in the minimum total heating. Stagnation-point heat-transfer rates were obtained as a function of nose radius for both an optically thin gas without radiation loss and a non-gray gas with radiation loss. The results of these solutions are presented in Figs. 13–16. The flight condition considered in Fig. 13 is typical of an Apollo-type entry. For this flight condition, the convective heating and the radiative heating are comparable in magnitude. These results include the effect of mass injection. The minimum nose radius from an optically thin analysis is slightly less than 2 ft. For a non-gray gas analysis with radiation loss, the minimum nose radius is seen to be greater than 4 ft. Also note that the total heating is a weak function of the nose radius for the non-gray gas. These results also show that the convective heating is little affected by self-absorption and radiation loss.

The flight conditions for Fig. 14 are again typical of an Apollo-type entry but at a higher altitude than the altitude considered in Fig. 13. For this condition, the convective heating is much larger than the radiative heating. These results do not include the effect of mass injection. For this case, self absorption has a somewhat smaller effect on the nose radius for the minimum total heating since the radiation is a small fraction of the total heating.

In Fig. 15, conditions typical of those encountered by a vehicle returning from Mars and entering the earth's atmosphere are considered. These results do not include the effect of mass injection. The nose radius which results in the minimum total heating for an optically thin gas without radiation loss is seen to be less than 1 ft. For a non-gray gas with radiation loss, this minimum nose radius is approximately 4 ft. The total heat flux is also seen to be a very weak function of the nose radius. For small nose radii, the combined effect of radiation loss and self-absorption is seen to decrease the convective heating slightly. For large nose radii, self-absorption becomes larger than the radiation cooling, and the convective heating is slightly increased. Similar

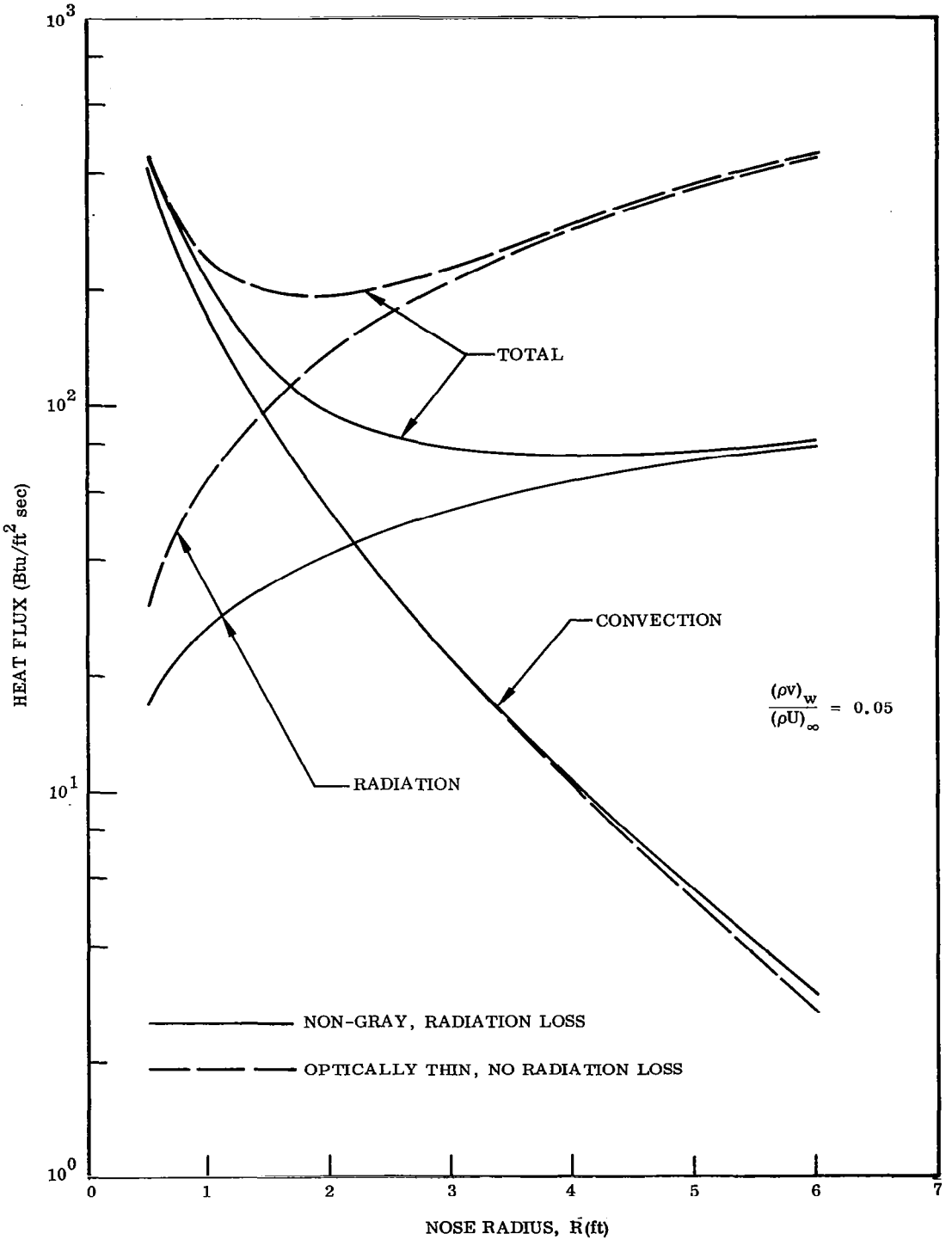

Fig. 13 Heat Flux as a Function of Nose Radius, $\bar{U} = 3.45$, $\bar{h} = 2.0$, With Mass Injection, $(\rho v)_W/(\rho U)_\infty = 0.05$

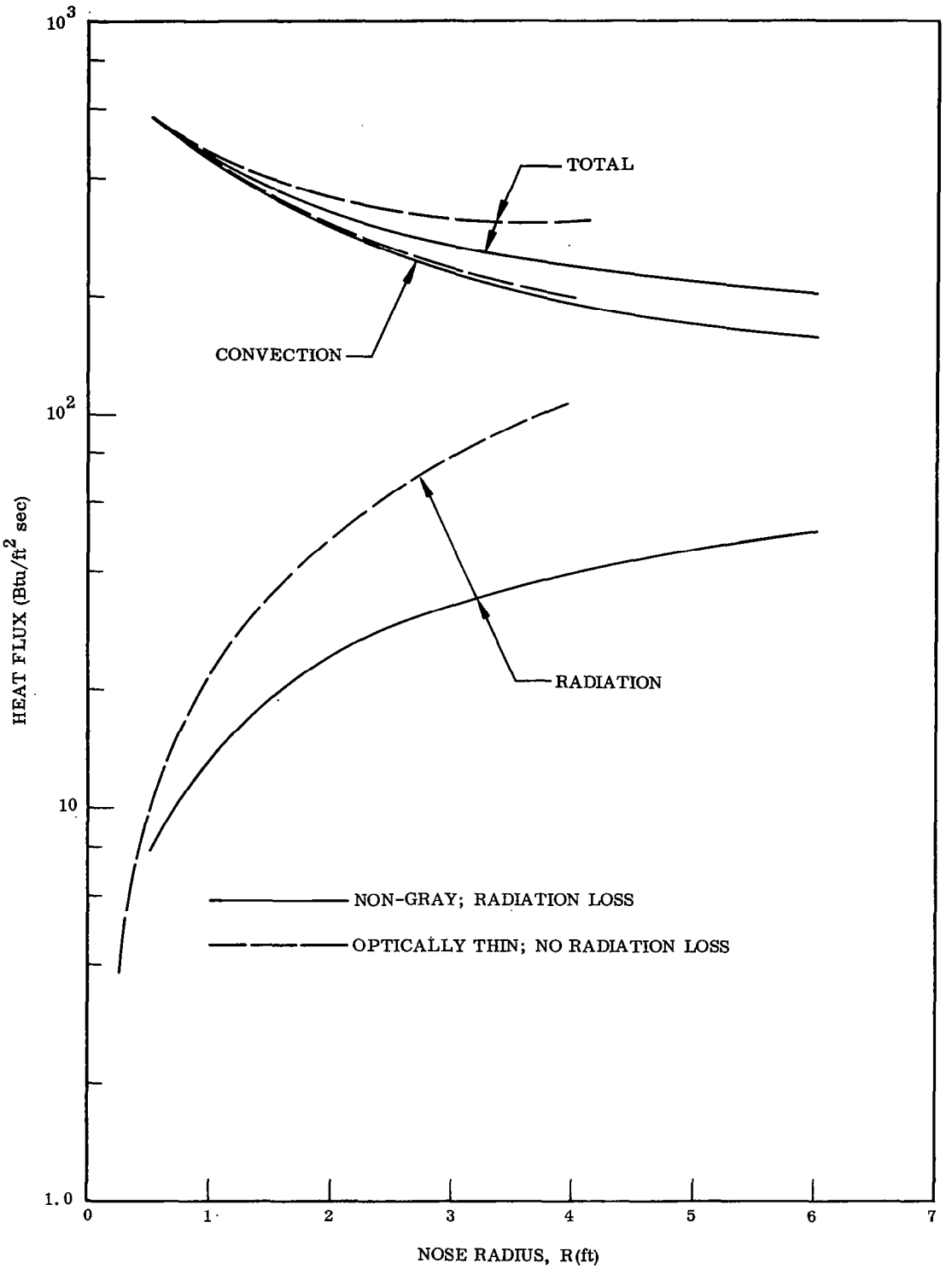

Fig. 14 Heat Flux as a Function of Nose Radius, $\bar{U} = 3.7$, $\bar{h} = 2.3$, No Mass Injection

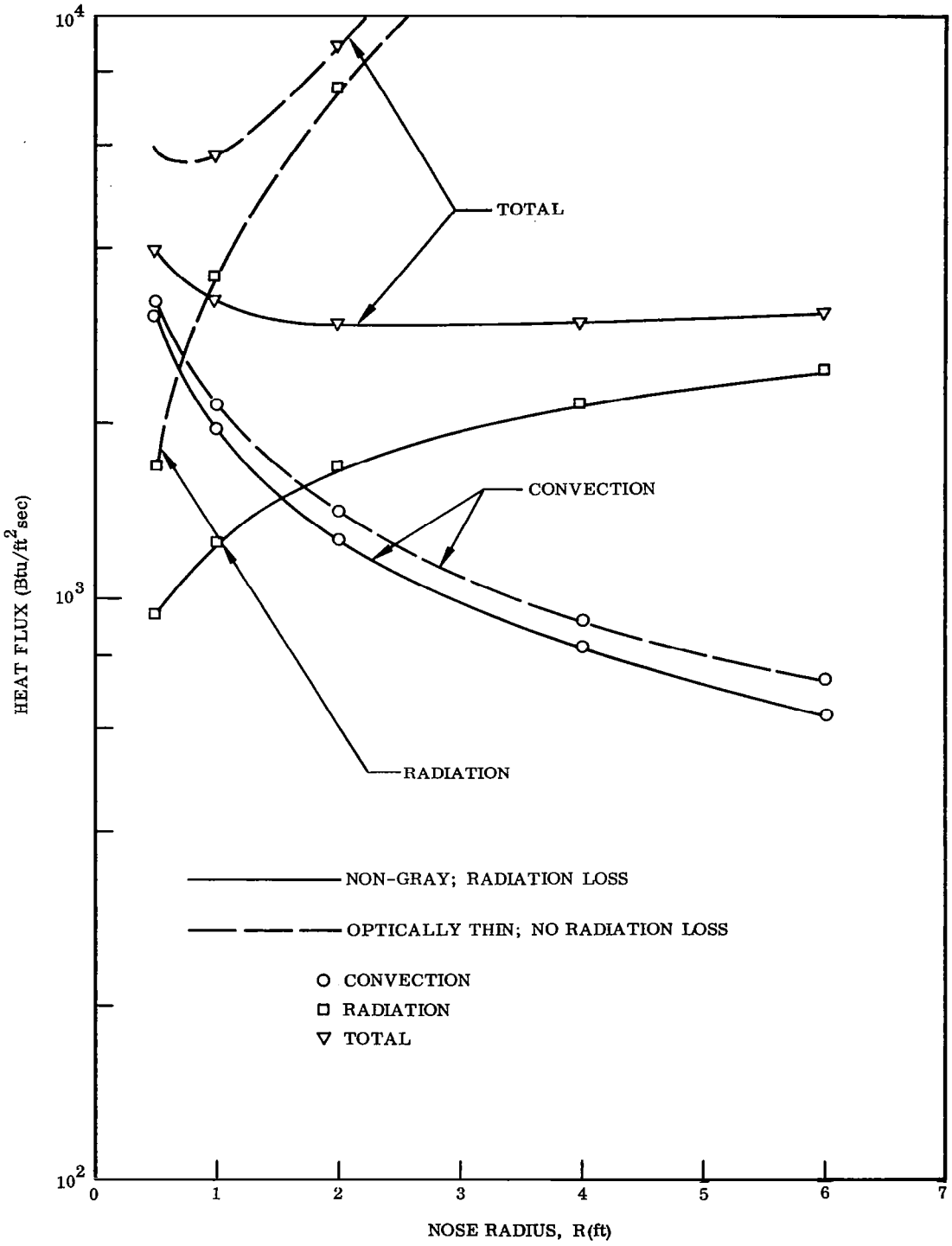

Fig. 15 Heat Flux as a Function of Nose Radius, $\bar{U} = 5.0$, $\bar{h} = 2.0$, No Mass Injection

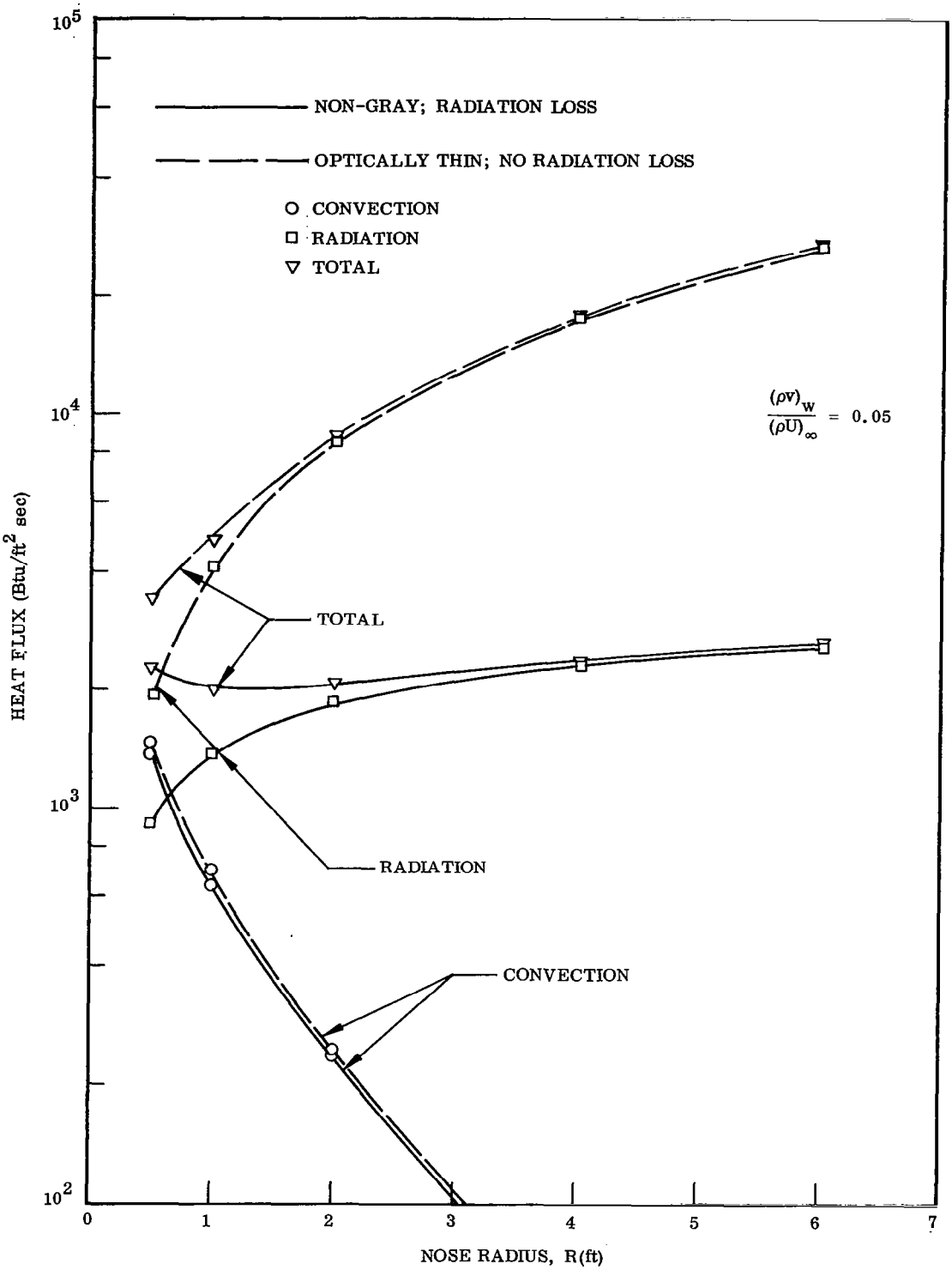

Fig. 16 Heat Flux as a Function of Nose Radius, $\bar{U} = 5.0$, $\bar{h} = 2.0$, With Mass Injection, $(\rho v)_w/(\rho U)_\infty = 0.05$

results are presented in Fig. 16 for the case of mass injection. The minimum nose radius for an optically thin gas is about 0.5 ft. For a non-gray gas the minimum nose radius is seen to be greater than 2 ft.

These results clearly demonstrate that it is feasible to design blunt entry bodies for missions which result in superorbital entry velocities. The common conclusion that the radiative heating will become overwhelming for large bodies at high flight velocities is seen to be false. Self-absorption reduces the radiative heating significantly and causes the radiative heating to vary approximately as the square root of the nose radius. Since the convective heating varies inversely as the square root of the nose radius, the total heating becomes a very weak function of the nose radius. One can increase the nose radius by factors of 2 to 3 without significantly affecting the total heat transfer.

The vehicle shape to be used for a particular mission should not be based solely on the results of this nature, but should include consideration of the total vehicle size and the dependence of the entry trajectory on vehicle shape.

5.4 HEAT TRANSFER DISTRIBUTION

The convective and radiative heat transfer distributions on a hemisphere are presented in Fig. 17 for a typical entry condition. These results were obtained from the first iteration (concentric shock) for both an optically thin gas without radiation loss and for a non-gray gas with radiation loss. For the flight condition considered, both the convective and radiative heat transfer distribution are insensitive to radiation cooling and spectral effects. At higher flight velocities and for larger bodies, these effects will be more significant.

The effect of shock shape iterations on the convective and radiative heat transfer distributions is shown in Fig. 18. The input and output values of the quantity ϵ, which is the difference between the body and shock angle, is also shown in Fig. 18. This quantity is used to measure the degree of convergence. It is seen that for the case

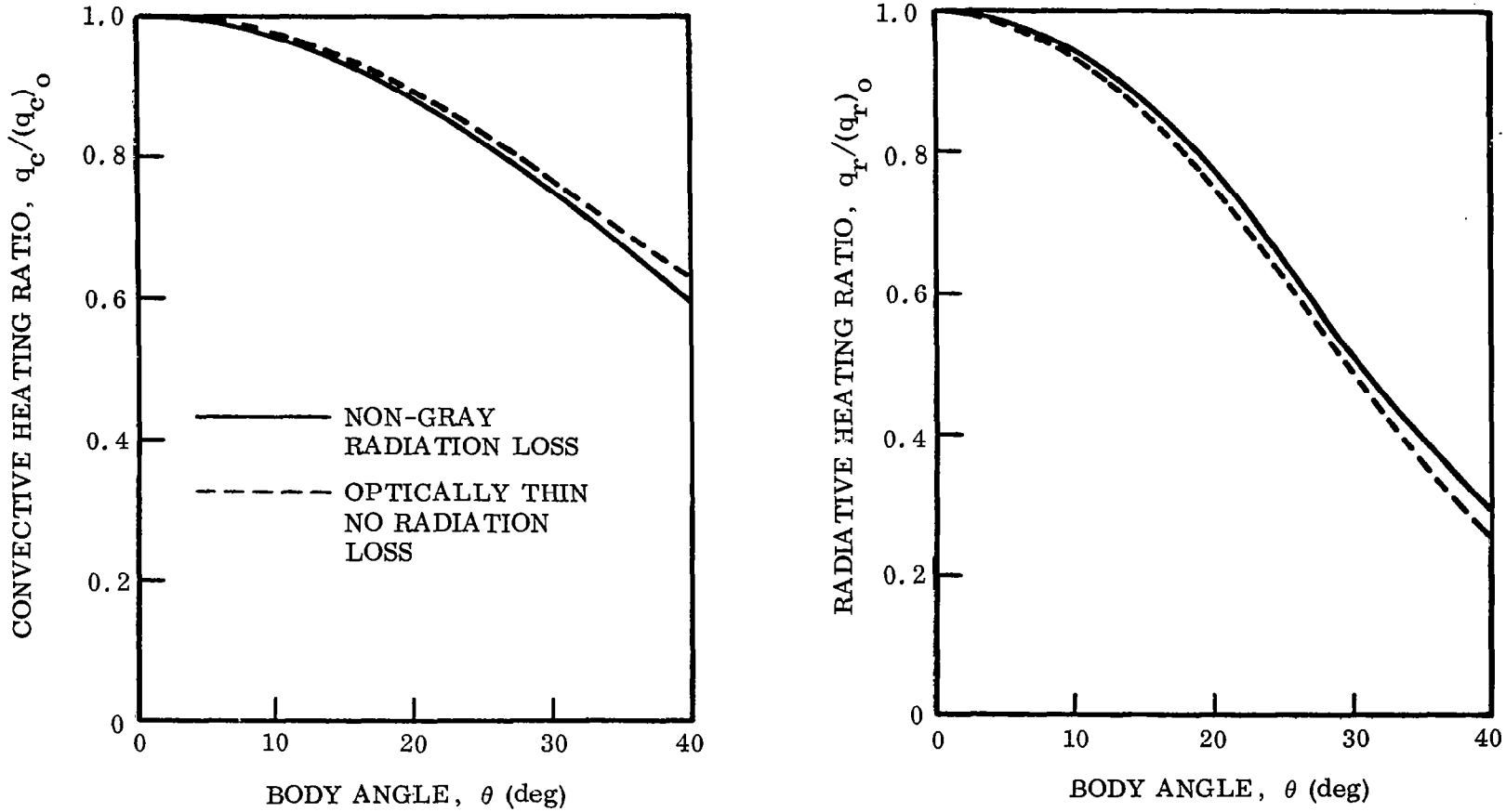

Fig. 17 Convective and Radiative Heat-Transfer Distribution on a Hemisphere, $\bar{U} = 4.1$, $\bar{h} = 1.8$, $R = 1$ ft, 1st Iteration

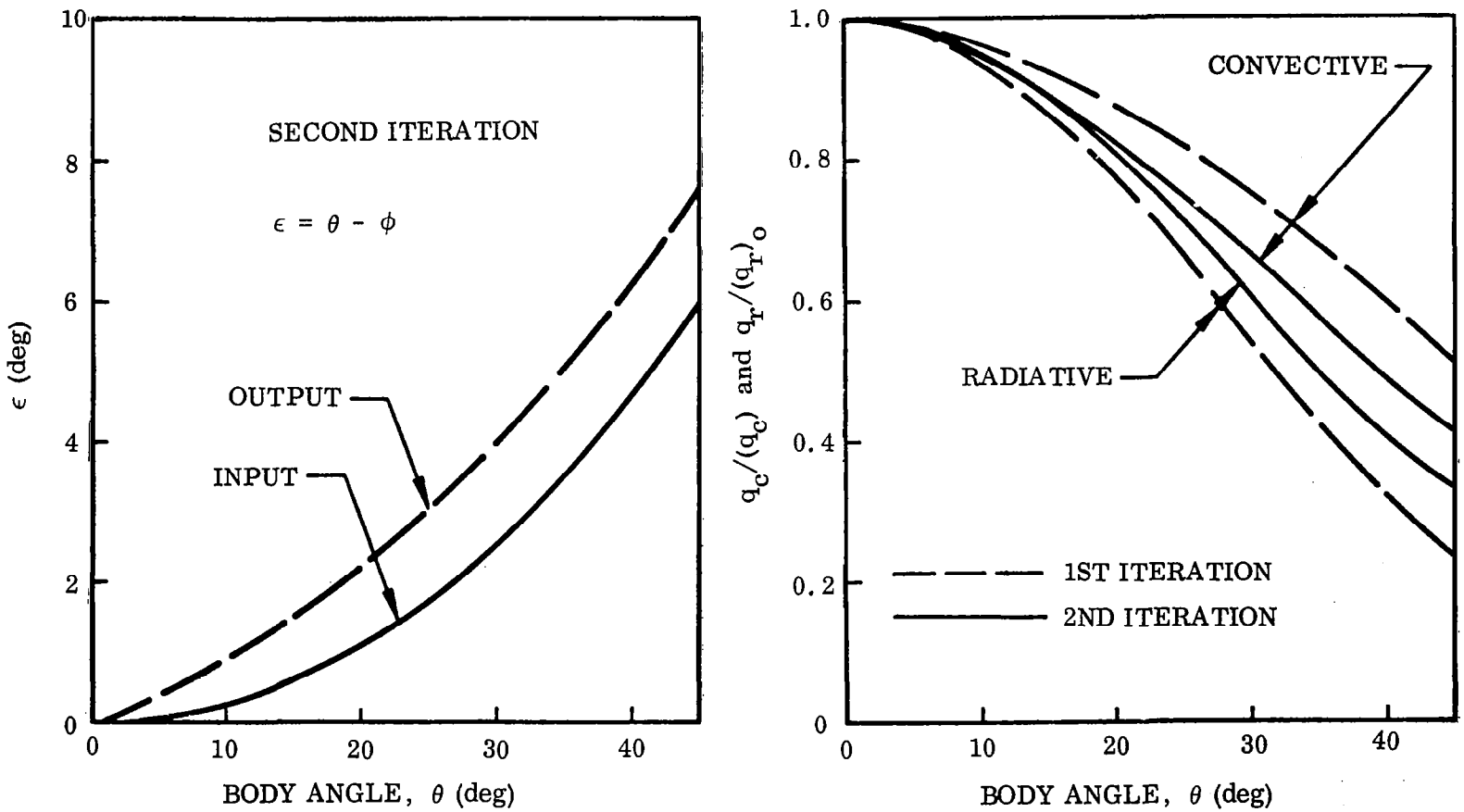

Fig. 18 Effect of Iteration on Heat-Transfer Distribution

shown in Fig. 18, the shock angle has converged to within 1.5 degrees. In the first iteration the shock angle is set equal to the body angle. A comparison of the results obtained from the first and second iterations shows that the radiative heating is increased slightly while the convective heating is slightly decreased. This decrease in the convective heating is due partly to the fact that in the first iteration, the pressure across the shock layer is assumed constant while in subsequent iterations, the y-momentum equation is solved in an approximate manner to determine the pressure variation across the shock layer.

The results presented in Fig. 17 are for a constant wall temperature (1450°K) whereas the first iteration results in Fig. 18 are for a variable wall temperature. Hence, the first iteration results in Figs. 17 and 18 differ slightly.

Section 6
CONCLUSIONS

The following conclusions are derived from the results of this analysis:

- The combined effect of radiation cooling and self-absorption results in a significant reduction in the radiative flux to the surface.
- The combined effect of radiation cooling and self-absorption has a small effect on the convective heat transfer.
- The absorption of radiative energy by molecules in the boundary layer slightly increases the convective heat transfer and slightly decreases the radiative heat transfer.
- The nose radius which results in the minimum total heat-transfer rate at the stagnation point is approximately 3 to 5 ft for the superorbital flight conditions considered.
- The radiative flux from an emitting and absorbing gas varies approximately as the square root of the nose radius, so that the total (convective plus radiative) heat rate is a weak function of the nose radius.

Section 7
REFERENCES

1. H. Hoshizaki and K. H. Wilson, "The Viscous, Radiating Shock Layer About a Blunt Body," AIAA Journal, Vol. 3, No. 9, Sep 1965, pp. 1614–1622

2. A. M. O. Smith and N. A. Jaffe, "General Method for Solving the Non-Equilibrium Boundary-Layer Equations of a Dissociating Gas," AIAA Paper No. 65-129, AIAA 2nd Aerospace Sciences Meeting, New York, New York, Jan 1965

3. S. M. Scala, "The Equations of Motion in a Multicomponent Chemically Reacting Gas," Aerophysics Operation Research Memo. 5, General Electric Co., Missile and Ordnance Systems Dept., Philadelphia, Pa., 1957

4. H. Hoshizaki, "Some Aspects of Radiation Transfer During Hypervelocity Reentry," Proceedings of the Workshop on the Interdisciplinary Aspects of Radiation Transfer, Joint Inst. for Lab. Astro., Univ. of Colo., 11, 12 Feb 1965, p. 6

5. C. F. Hansen, "Approximations for the Thermodynamic and Transport Properties of High-Temperature Air," NASA TR R-50, 1959

6. J. R. Viegas and J. T. Howe, "Thermodynamic and Transport Property Correlation Formulas for Equilibrium Air From 1,000°K to 15,000°K," NASA TN D-1429, Oct 1962

7. Gerhard Herzberg, F.R.S., Molecular Spectra and Molecular Structure, Second Edition, Eighth Printing, Princeton, New Jersey, Van Nostrand, Feb 1963, pp. 315

8. R. E. Meyerott, J. Sokoloff, and R. W. Nicholls, "Absorption Coefficients of Air," Geophysical Research Paper 58, GRD-TN-60-277, Jul 1960

9. John S. Evans and Charles J. Schexnayder, Jr., "An Investigation of the Effect of High Temperature on the Schumann-Runge Ultraviolet Absorption Continuum of of Oxygen," NASA Technical Report R-92, 1961

10. R. A. Allen, A. Textoris, and J. Wilson, "Measurements of the Free-Bound and Free-Free Continua of Nitrogen, Oxygen and Air," Journal of Quantitative Spectroscopy and Radiative Transfer, Jan–Feb 1965

11. L. M. Biberman and G. E. Norman, "Recombination Radiation and Bremsstrahlung of a Plasma (Free-bound and Free-free Electron Transitions in a Field of Positive Ions)," Journal of Quantitative Spectroscopy and Radiative Transfer, Vol. 3, 1963, pp. 221–245

12. B. H. Armstrong, S. Brush, H. DeWitt, R. R. Johnston, P. S. Kelley, and O. R. Platas, "Opacity of High Temperature Air," Air Force Weapons Laboratory, Final Report under Contract AF 29(601)-5006 (to be issued)

13. B. H. Armstrong, Private communication

14. R. W. Nicholls, "Laboratory Astrophysics," Journal of Quantitative Spectroscopy and Radiative Transfer, Vol. 2, Oct–Dec 1962, pp. 433–449

15. W. E. Nicolet, private communication

16. James O. Arnold, Victor H. Reis, and Henry T. Woodward, "Theoretical and Experimental Studies of Equilibrium and Nonequilibrium Radiation to Bodies Entering Postulated Martian and Venusian Atmospheres at High Speeds," AIAA Paper No. 65-116, AIAA 2nd Aerospace Sciences Meeting, New York, New York, 25–27 Jan 1965

17. P. J. Marteney and N. L. Krascella, "Theoretical and Experimental Investigations of Spectral Opacities of Mixtures of H Hydrogen and Diatomic Cases," Research and Technology Division, Edwards Air Force Base, Calif., RTD-TDR-63-1102, Nov 1963

18. G. E. Norman, "Photoionization Cross Section of the Lower Excited States and Oscillator Strengths of Certain Lines of Carbon and Nitrogen Atoms," Optics and Spectroscopy, Vol. XIV, No. 5 (1963)

19. D. R. Bate and M. J. Seaton, "The Quantal Theory of Continuous Absorption of Radiation by Various Atoms in Their Ground States," Mon. Notices, Roy. Astron. Soc., 109 (1949)

20. H. Hoshizaki, "Heat Transfer in Planetary Atmospheres at Super-Satellite Speeds," ARS J., Oct 1962

21. John T. Howe and Yvonne S. Sheaffer, "Mass Addition in the Stagnation Region for Velocity Up to 50,000 Feet Per Second," NASA Technical Report NASA TR R-207, Aug 1964

NASA-Langley, 1966 CR-584

"The aeronautical and space activities of the United States shall be conducted so as to contribute . . . to the expansion of human knowledge of phenomena in the atmosphere and space. The Administration shall provide for the widest practicable and appropriate dissemination of information concerning its activities and the results thereof."

—NATIONAL AERONAUTICS AND SPACE ACT OF 1958

NASA SCIENTIFIC AND TECHNICAL PUBLICATIONS

TECHNICAL REPORTS: Scientific and technical information considered important, complete, and a lasting contribution to existing knowledge.

TECHNICAL NOTES: Information less broad in scope but nevertheless of importance as a contribution to existing knowledge.

TECHNICAL MEMORANDUMS: Information receiving limited distribution because of preliminary data, security classification, or other reasons.

CONTRACTOR REPORTS: Technical information generated in connection with a NASA contract or grant and released under NASA auspices.

TECHNICAL TRANSLATIONS: Information published in a foreign language considered to merit NASA distribution in English.

TECHNICAL REPRINTS: Information derived from NASA activities and initially published in the form of journal articles.

SPECIAL PUBLICATIONS: Information derived from or of value to NASA activities but not necessarily reporting the results of individual NASA-programmed scientific efforts. Publications include conference proceedings, monographs, data compilations, handbooks, sourcebooks, and special bibliographies.

Details on the availability of these publications may be obtained from:

SCIENTIFIC AND TECHNICAL INFORMATION DIVISION

NATIONAL AERONAUTICS AND SPACE ADMINISTRATION

Washington, D.C. 20546